Engineering Journal

First Quarter 2025 | Volume 62, No. 1

Smarter.
Stronger.
Steel.

Engineering Journal

American Institute of Steel Construction

Dedicated to the development and improvement of steel construction, through the interchange of ideas, experiences, and data.

Editorial Staff

Editor	Margaret A. Matthew, PE
Managing Editor	Keith A. Grubb, SE, PE
Research Editor	Judy Liu, PhD
Production Editor	Kristin Hall

Officers

Chair
Hugh J. McCaffrey

Vice Chair
Glenn R. Tabolt

Secretary/Legal Counsel
Edward Seglias

President
Charles J. Carter, SE, PE, PhD

Senior Vice Presidents
Scott L. Melnick
Mark W. Trimble, PE

Vice Presidents
Todd Alwood
Brandon Chavel, PE, PhD
Carly Hurd, CAE
Christopher H. Raebel, SE, PE, PhD
Michael Mospan
Brian Raff

The articles contained herein are not intended to represent official attitudes, recommendations or policies of the Institute. The Institute is not responsible for any statements made or opinions expressed by contributors to this Journal.

The opinions of the authors herein do not represent an official position of the Institute, and in every case the officially adopted publications of the Institute will control and supersede any suggestions or modifications contained in any articles herein.

The information presented herein is based on recognized engineering principles and is for general information only. While it is believed to be accurate, this information should not be applied to any specific application without competent professional examination and verification by a licensed professional engineer. Anyone making use of this information assumes all liability arising from such use.

Manuscripts are welcomed, but publication cannot be guaranteed. All manuscripts should be submitted in duplicate. Authors do not receive a remuneration. Guidelines for authors are printed on the inside back cover.

Engineering Journal (ISSN 0013-8029) is published quarterly. Published by the American Institute of Steel Construction at 130 E Randolph Street, Suite 2000, Chicago, IL 60601.

Copyright 2025 by the American Institute of Steel Construction. All rights reserved. No part of this publication may be reproduced without written permission. The AISC logo is a registered trademark of AISC.

Archives: Search at **aisc.org/ej**.
Article downloads are free for current members and are available for a nominal fee for non-members.

Letter from the Editor

Dear Readers,

Happy New Year! At the start of this shiny new year, I would like to recognize all the hard work of our many reviewers, last year and every year. Their contributions are invaluable to the success of the *Journal* as we continue to strive to bring you the very best articles and information in the steel construction industry.

Is there a steel design topic you would like to see in *EJ*? We are always looking for ideas for papers. Authors interested in submitting papers should visit our website at www.aisc.org/ej for author guidelines and submittal information.

Best wishes for a healthy and happy 2025!

Sincerely,

Margaret A Matthew

Margaret A. Matthew, P.E.
Editor

Load-Dependent Critical Temperatures for Standard Fire Resistance of W-Shape Floor Beam Assemblies: Experimental Validation and Simplified Analysis

MICHAEL M. DRURY and SPENCER E. QUIEL

ABSTRACT

Comprehensive results of ASTM E119 (2019) standard fire tests (performed by AISC/AISI in 2015) are used to validate load-dependent critical temperature relationships that conservatively predict the thermally induced loss of flexural resistance for W-shape floor beam assemblies. The 16 tested assemblies used the same W8×28 section (coated with the same thickness of passive spray-applied fire resistive material), supported 2½ in. (64 mm) of lightweight concrete (reinforced with welded wire mesh) on a 2 in. (51 mm) corrugated metal deck, and had a clear span of 154¾ in. (3.93 m) in one-way bending. Four specimen groups in the following configurations were tested with four specimens each: restrained ends with composite slab, unrestrained ends with composite slab, restrained ends with noncomposite slab, and unrestrained ends with noncomposite slab. The four specimens in each group were each tested with a constant applied flexural load but at a range of magnitudes, inducing maximum bending moment from 23 to 60% of the section's ambient nominal moment capacity. The results of these tests clearly demonstrate a relationship between the loss of flexural resistance and the increase in steel beam temperature (particularly the bottom flange temperature) as a function of applied loading. The fire-induced temperature increases in the protected steel beams are then used to validate lumped mass thermal calculations per the AISC *Specification* (2022) and Part 1-2 of Eurocodes 3 and 4 (CEN, 2005, 2008), which are classified as simple analysis methods per Section A-4.2.4d of the AISC *Specification*. The results of this study demonstrate that simplified thermal analysis methods can be combined with load-dependent critical temperature relationships to conservatively predict the standard fire resistance of W-shape floor beam assemblies at the onset of flexural failure.

Keywords: standard fire resistance design (SFRD), W-shape steel floor beam assembly, composite vs. noncomposite slab, restraint of thermal expansion, critical steel temperature at flexural runaway, hourly fire resistance ratings.

INTRODUCTION

Floor systems in North American steel-framed building construction are often comprised of wide-flange (i.e., W-shape) beams that support a concrete slab. Beams that are not part of a moment-resisting frame are typically designed as one-way simple spans that are supported by shear connections. The slab is typically reinforced with steel bars or welded wire reinforcement (WWR) and is cast onto corrugated or fluted light-gage metal decking. The beam and slab are often constructed to be composite at their interface, thus achieving a degree of strain compatibility and amplifying their collective flexural stiffness and moment capacity. Composite action is commonly developed by welding headed shear studs at regularly spaced intervals through the metal deck to the top flange of the beam prior to concrete placement (see Figure 1).

Floor beams often require the application of passive fire protection to meet minimum hourly fire resistance ratings as a function of the building's size, occupancy, and purpose per the International Building Code (IBC) (ICC, 2020). Passive fire protection for W-shape beams in current practice often consists of spray-applied fire-resistive material (SFRM), which is a lightweight cementitious product with high thermal resistance. Due to their sheer quantity, floor beams can require a significant portion of the overall amount of SFRM applied to all steel framing throughout the building. Hourly fire resistance ratings describe the time needed to exceed a thermal or structural limit criterion when the assembly is subjected to a "standard fire" heating regime, such as those provided in ASTM E119 (2019), UL 263 (2020), or ISO 834 (2019). As shown in Figure 2, these temperature time histories undergo a rapid rise during the first 10 min, after which the rate of temperature increase slows before approaching 2000°F (1093°C) after 3 hr. Beyond that time, these high temperatures would continue to gradually increase with no subsequent decay phase or any consideration of suppression from sprinklers (i.e., active fire protection). The initial 2 hr period of a standard fire curve is intended to generally represent the ramp-up of temperature in a post-flashover building compartment, and

---

Michael M. Drury, Associate, Wiss, Janney, Elstner Associates, Inc., Princeton, N.J. Email: mdrury@wje.com

Spencer E. Quiel, Associate Professor, Department of Civil and Environmental Engineering, Lehigh University, Bethlehem, Pa. Email: seq213@lehigh.edu (corresponding)

Paper No. 2023–11R

ISSN 2997-4720

the indefinite continuation of high temperature exposure will ensure that the thermal and/or structural performance criteria limits are eventually reached.

For comparison, a “natural” fire temperature time history would increase as a function of the geometry, fuel load, ventilation, and material characteristics of a given building compartment (CEN, 2009) and then eventually enter a subsequent decay phase until burnout. A representative natural fire curve from a previous study by the authors (Drury and Quiel, 2023a) is plotted for comparison in Figure 2. A natural fire curve can be used to evaluate the survivability and resilience of a structural assembly to a realistic fire exposure. Such considerations are outside the scope of this paper, but the reader is referred to several recent publications by ASCE for more guidance (ASCE, 2020; LaMalva, 2018).

In a typical standard fire evaluation, a floor beam assembly (which includes a supported slab) with an SFRM-protected W-shape section is heated from below while carrying a flexural load. Standard fire tests for floor beam assemblies are conducted as either restrained (i.e., the ends of the beam are fully restricted from axial thermal expansion or rotation) or unrestrained (i.e., the beam ends are free to thermally expand and rotate). These idealized configurations do not represent actual boundary conditions in a building but are intended to bracket the partial restraint

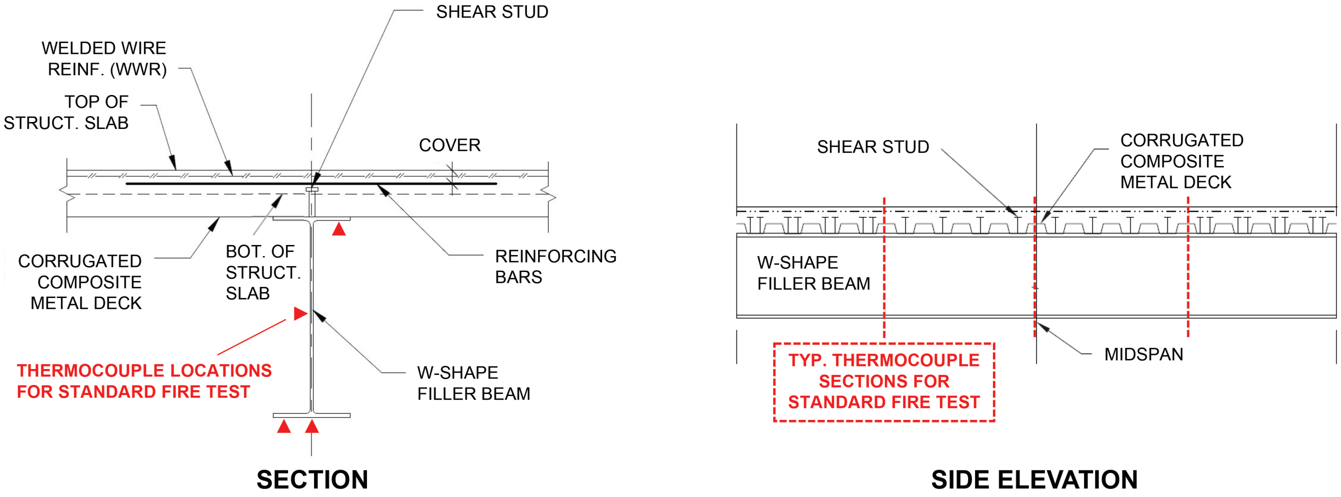

Fig. 1. Representative illustration of a composite W-shape floor beam, including thermocouple placement for an ASTM E119 standard fire test.

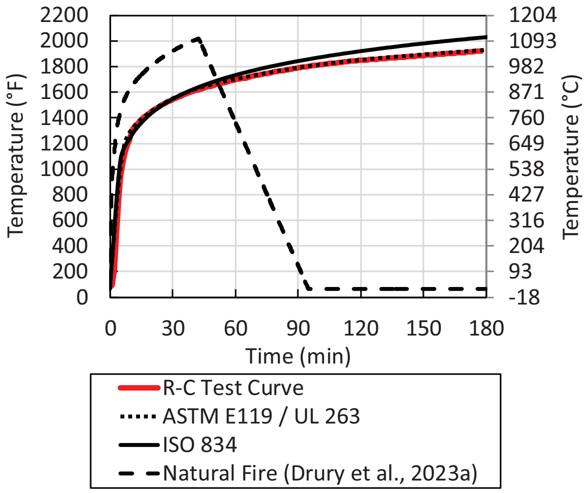

Fig. 2. Comparison of the R-C test’s furnace temperature time history with select standard and natural fire curves.

Table 1. Temperature and Deflection Performance Limits per Published Standards for Standard Fire Testing of W-Shape Floor Beam Assemblies

Type of Limit	Source	Limit
Midspan deflection	ASTM E119-19	• Midspan deflection: $L^2/(400d)$ THEN • Deflection rate per minute: $L^2/(9000d)$
	BS 476-21:1987	• Midspan deflection: $L/20$
Critical temperature of steel beam	ASTM E119-19	• Average steel beam temperature from 4 thermocouples per Figure 1 ($T_{s,E119}$): 1100°F (593°C) AND • Maximum steel beam temperature at a single thermocouple ($T_{s,MAX}$): 1300°F (704°C)
Critical temperature transmission through slab	ASTM E119-19	• Average temperature increase above ambient at the unexposed top-of-slab surface: 250°F (139°C) AND • Maximum temperature increase above ambient at any point on the unexposed top-of-slab surface: 325°F (181°C)

to thermal expansion and end rotation that would be provided by realistic connections and a continuous reinforced concrete floor slab. The heated assembly is monitored for its ability to sustain the applied flexural load as well as for the temperature increase in the steel beam and thermal transmission through the concrete slab. The time at which a given criteria is met is then rounded down to the nearest half-hour to denote the hourly fire resistance rating for the tested section configuration. Standard fire resistance design (SFRD), which is widely used in current practice, uses these hourly ratings as a comparative indicator of ultimate capacity under a standardized fire exposure.

Table 1 summarizes the thermal and structural performance limit criteria that are used to signify "failure" during a standard fire test of a composite steel floor beam. The deflection limits per ASTM E119 (2019) or BS 476 (BSI, 2008, 1987) are intended to represent a loss of flexural resistance (i.e., at or near the onset of runaway failure) and are calculated as a function of the clear span of the beam, L, and the distance between the extreme fibers of the cross section in compression and tension, d, which includes the slab thickness and depth of the fluted deck for a composite section (Alfawakhiri et al., 2016; Drury and Quiel, 2023b, 2023a). In a standard fire test per ASTM E119, temperatures are measured at a minimum of three sections along the length of the specimen, with four thermocouples at each section as shown in Figure 1. The maximum temperature limit per ASTM E119 is evaluated against the maximum reading among all thermocouples on the steel beam.

Because the bottom flange has the greatest exposure to fire among these three plates, one of its thermocouples often indicates the section's maximum temperature. The top flange temperature, $T_{s,TF}$, typically remains cooler than that of the web, $T_{s,web}$, and bottom flange, $T_{s,BF}$, calculated as an average of its two thermocouples because its upper surface is in contact with the supported floor slab, thus partially shielding it from heating. $T_{s,BF}$ and $T_{s,web}$ are often similar, with $T_{s,BF}$ being more critical to flexural strength. For the other ASTM E119 thermal limit, a weighted average temperature, $T_{s,E119}$, over a given cross section is calculated as a simple average of all four thermocouple measurements at that section. $T_{s,E119}$ will therefore trend hotter than a true area-weighted average value due to the placement of two thermocouples on the bottom flange and only one each on the other plates (Drury et al., 2020).

The results of standard fire tests are compiled in catalogs such as the UL *Fire Resistance Directory* (2019a). Due to the size limitations of most available furnaces, standard fire tests are usually conducted on floor beam assemblies with shorter spans (10–17 ft) and use a relatively small W-shape section (such as a W8×28 or W12×14). SFRM thicknesses needed for larger sections in actual construction can be calculated using Appendix 4 of the AISC *Specification* (2022), with additional guidance and examples available in ASCE 29-05 (2007) and AISC Design Guide 19 (Ruddy et al., 2003). These resources provide semi-empirical conversion equations based on the relative ratio of cross-sectional area to fire-exposed perimeter between the actual floor beam and the tested specimen from the rated assembly. These methods are implemented as qualification testing per of AISC *Specification* Section A-4.3 and provide a straightforward translation of tested fire resistance to a steel floor beam design.

As an alternative to the prescriptive application of qualification test results, IBC Section 703.2.2.4 (ICC, 2020) permits the use of engineering analysis to demonstrate an equivalent fire resistance rating as required in Table 601 for an actual member or assembly. To pursue this option, the designer would need adequate thermal and structural information about the setup and outcome of a standard fire test, with which the analysis approach could be validated for the tested specimen. Once validated, the analysis approach could then be applied to a model of the actual assembly (with expected loading and realistic boundary conditions), and a so-called virtual standard fire test would be conducted to determine equivalency to the tested fire resistance rating. However, there are a few significant challenges when attempting to use standard fire test outcomes in this way:

- Per Section 7.4.4.1 of ASTM E119 (2019), the applied flexural loading should represent "the maximum load condition allowed under nationally recognized structural design criteria unless limited design criteria are specified and a corresponding reduced load is applied." Appendix X7 of ASTM E119 states that fire resistance tests have been historically conducted using loads based on maximum allowable stresses. However, the exact load used to test a floor beam assembly is rarely reported in the corresponding fire resistance rating. Variations in assumed material strengths can lead to a range of loads being considered as "the maximum load condition." Also, the flexural design of floor beams at ambient conditions is often governed by serviceability limits rather than by strength. Current application of the ASTM E119 test results in practice do not account for realistic variability of design loading and flexural utilization (which can be calculated as the ratio of applied moment to nominal ambient moment capacity, M/M_n) for realistic floor beam designs. Also, ASTM E119 does not provide any load-based correlation between the thermal and structural performance limits in Table 1.
- The evolution of standard fire testing over time has produced terminology and testing procedures that can be challenging to understand if someone is not intimately familiar with the testing process. Per Table X3.3 of ASTM E119 (2019), hourly ratings for steel floor beams that support concrete slabs can be obtained from four different testing configurations: restrained assembly, unrestrained assembly, restrained beam, and unrestrained beam. Assembly tests also limit thermal transmission through the slab to its unexposed top face, and a restrained beam test does not require the slab edge above the end of the beam to also be restrained (i.e., only the end of the steel beam itself is restrained). Several classifications of hourly ratings can be obtained from a single test when using some of these testing configurations (Berhinig and Alfawakhiri, 2014; Bono, 1970; LaMalva et al., 2020; Ruddy et al., 2003). For example, a single restrained assembly test can be used to obtain a restrained assembly, unrestrained assembly, and an unrestrained beam rating by applying the varied thermal and structural criteria limits to the single set of test data. An unrestrained beam rating that is extrapolated from a restrained assembly test has slightly different performance limits than that obtained directly from a true unrestrained beam test. Despite this, the published listings of fire resistance ratings for floor beam assemblies (UL, 2019a) do not typically clarify which test configuration was used or which criterion (thermal or structural) was exceeded to obtain a particular hourly rating.
- Per AISC *Specification* Section A-4.3.1 (2022), demonstrating equivalency to a standard fire resistance rating is only permitted via "advanced methods of analysis" as described in Section A-4.2.4c of the same document. These advanced methods typically use finite element (FE) thermal and structural models to evaluate structural fire response. Expertise and project resources (namely, time and budget) are needed to conduct these FE analyses, and the benefits offered by such an approach (either in terms of enhanced performance or fire protection cost savings) must outweigh the costs associated with the design effort. The simple methods of analysis per Section A-4.2.4d, or the recently added critical temperature method per Section A-4.2.4e would be a more accessible tool for tailoring standard fire resistance ratings to realistic floor beam assemblies; however, these approaches are not currently permitted by the AISC *Specification* for this application. Currently, no provisions exist in Section A-4.2.4e related to determining the fire resistance of floor beam assemblies.

In an effort to simplify the determination of equivalent fire resistance for W-shape floor beams, researchers with AISC and AISI performed 16 ASTM E119 standard fire tests in 2015 for which the steel beam was protected with a contoured coating of SFRM (Alfawakhiri et al., 2016). The results of these tests were used to develop the inaugural UL D982 assembly listing (UL, 2019b) and are reproduced in this paper with permission from AISC. All specimens used the same W8×28 section, SFRM thickness, corrugated concrete slab characteristics, and span geometry. Four specimen groups in the following configurations were tested with four specimens each: restrained ends with composite slab (R-C), unrestrained ends with composite slab (U-C), restrained ends with noncomposite slab (R-NC), and unrestrained ends with noncomposite slab (U-NC). The four specimens in each group were each tested with a constant applied flexural load but at a range of magnitudes, inducing a maximum moment, M, ranging from 23–60% of nominal flexural strength, M_n. The results of those tests are used in this paper to illustrate the relationship between flexural response and the increase in steel beam temperature as a function of applied loading. The results of other quasi-standard tests in the published literature will also be used to further demonstrate this relationship for a wider range of composite beam cross sections, span lengths, slab configurations, and boundary conditions.

The results of the AISC/AISI tests were used as validation for thermo-mechanical FE models in Chapter 6 of the doctoral dissertation by Drury (2022). The reader is directed to that reference for guidance on the implementation of advanced analysis per Section A-4.2.4c of the AISC *Specification* for developing equivalent standard fire resistance. This paper instead demonstrates the application of simple methods of thermal analysis per Appendix 4 of the AISC *Specification* as well as Part 1-2 of Eurocodes 3 and 4 (CEN, 2005, 2008) for predicting critical steel temperatures per the load-dependent relationship. The time at which those critical temperatures are reached under exposure to a standard fire curve could then be used to indicate an equivalent standard fire resistance.

LOAD-DEPENDENT CRITICAL TEMPERATURE RELATIONSHIPS

Existing Specifications

Load-dependent critical temperatures for steel beams are available in current design standards but do not necessarily target composite floor beams. For example, AISC *Specification* Section A-4.2.4e (2022) provides a critical temperature relationship, T_{cr}, for flexural yielding of a continuously braced beam not supporting a concrete slab as a function of the ratio of applied moment, M, versus the nominal flexural strength due to yielding at ambient temperature, M_n:

AISC *Specification* Equation A-4–23:

$$T_{cr} = 816 - 306 \ln\left(\frac{M}{M_n}\right) \text{ (in °F)} \tag{1}$$

Eurocode 3, Part 1-2 (CEN, 2005) provides a similar relationship for critical temperature, T_{cr}, of a generic steel section as a function of initial ambient flexural utilization, M/M_n:

Eurocode 3, Part 1-2, Equation 4.22:

$$T_{cr} = 39.19 \ln\left[\frac{1}{0.9674\left(\frac{M}{M_n}\right)^{3.833}} - 1\right] + 482 \text{ (in °C)} \tag{2}$$

Per both specifications, the values of T_{cr} from Equations 1 and 2 should be applied to the average temperature of the steel cross section, T_s. The plots in Figure 3 show that Equations 1 and 2 both provide similar relationships between T_{cr} and M/M_n for generic steel sections, with the AISC expression providing an approximate 5% conservative value.

Eurocode 4, Part 1-2 (CEN, 2008) permits the application of T_{cr} from Equation 2 as a limit for either T_s or $T_{s,BF}$ in a floor beam that supports a composite slab. The AISC *Specification* does not currently provide an explicit critical temperature relationship for floor beams that support a concrete slab; however, Table A-4.2.4 of the AISC *Specification* provides a flexural retention factor ($k_{cb} = M_{n,T}/M_n$) for composite beams as a function of $T_{s,BF}$ (which is intended to

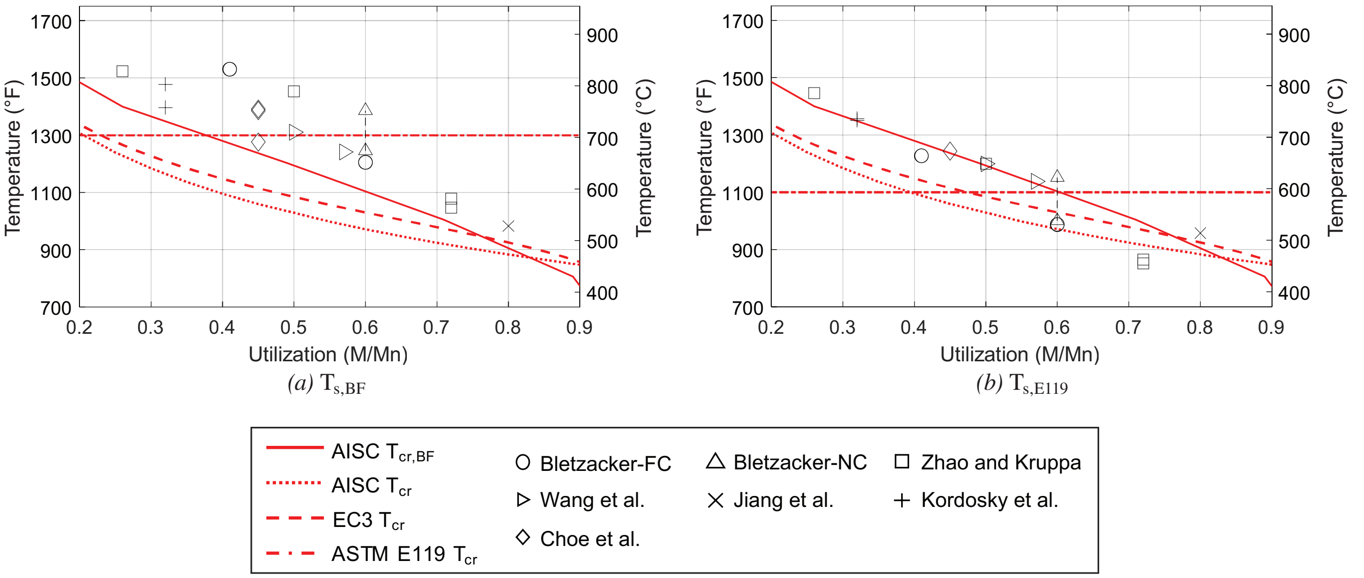

(a) $T_{s,BF}$ *(b)* $T_{s,E119}$

Fig. 3. Critical steel beam temperatures from the existing experimental literature as a function of initial ambient flexural utilization.

represent the maximum temperature of the steel section and govern its flexural resistance). The values in Table A-4.2.4 can be reframed as a function of critical bottom flange temperature, $T_{cr,BF}$, versus flexural utilization, M/M_n, and this relationship is plotted in Figure 3 for comparison. As would be expected, the values for the AISC $T_{cr,BF}$ per Table A-4.2.4 are greater than those for T_{cr} from Equations 1 and 2 up to a flexural utilization of ~75%. These critical temperature curves are compared against the results of quasi-standard fire testing from the published literature in the following section.

Comparison with Published Results of Quasi-Standard Fire Tests

Numerous studies have used a quasi-standard fire test to demonstrate a load-dependent relationship between steel beam temperature and one-way flexural performance of composite and noncomposite floor assemblies, thus supporting the notion that ultimate fire resistance can be correlated to a critical temperature. Table 2 lists seven experimental programs from 1967 to 2020 that tested one-way composite floor beams under a heating regime that either matched or closely resembled a standard fire curve. All tests used varied shear stud layouts to induce a broad range of composite action. Test parameters included both flat and profiled slabs (with varying compressive strengths and concrete unit weights), protected and unprotected steel beams (with varying steel grade, based on their construction era), lengths ranging from 11 to 40 ft (3.35–12.2 m), and varying degrees of axial and rotational end restraint (due to variation in the available support conditions for a particular furnace).

Though limited in some cases by laboratory-specific constraints to prevent damage to the furnace, the flexural failure criteria used for each study was generally similar to that shown in Table 1 and were intended to capture the moment at which the beam would no longer be able to carry the superimposed load. Flexural loading for each test was applied via multiple point loads to induce a maximum bending moment that equaled between 26 and 80% of the ambient (unfactored) moment capacity. Where nominal values were absent in the test reporting, reasonable strength assumptions were made based on the reported properties from material testing. For reference, expected flexural utilization in practice will range from 20 to 60% of the nominal moment capacity, with an upper limit of 70% being reached in rare design circumstances (Newman, 1999).

Nearly all test programs reported a full thermal profile of $T_{s,TF}$, $T_{s,BF}$, and $T_{s,web}$ in the steel beam at failure, with the exception of tests CB-SP and CB-DA-SC per Choe et al. (2020) (which only reported a bottom flange or maximum temperature due to thermocouple malfunctions during testing). The reported temperatures were used to identify $T_{s,BF}$ and calculate $T_{s,E119}$ at the time of flexural failure per the criteria defined in each study, and the results are plotted as a function of initial ambient flexural utilization in Figure 3. The experimentally measured values of critical $T_{s,BF}$ in Figure 3(a) shows slightly greater dispersion than the corresponding critical $T_{s,E119}$ in Figure 3(b), which suggests that a more consistent result may be obtained when web and top flange temperatures are also incorporated in the critical temperature evaluation. Both plots clearly show that the existing flat critical temperature limits per ASTM E119 are unable to capture the test results across variations in applied loading. Both AISC *Specification* Equation A-4-23 (Equation 1) and the Eurocode critical temperature per Equation 2 provide a good correlation to critical $T_{s,E119}$ across all tests in Figure 3(b). In particular, AISC *Specification* Equation A-4-23 provides a lower bound to most of the test data, with the only exception being the Zhao and Kruppa (1997) results at a flexural utilization ratio of 0.72 (which is above a realistic upper bound of 0.6 for flexural utilization at service levels). The curves for T_{cr} per Equations 1 and 2 provide an unnecessarily conservative prediction of critical $T_{s,BF}$ in Figure 3(a); however, the $T_{cr,BF}$ based on Table A-4.2.4 of the AISC *Specification* provides a reasonably conservative best prediction across all data points. In the next section, these curves will be further evaluated against the results of the aforementioned 16 standard fire tests by Alfawakhiri et al. (2016).

STANDARD FIRE TESTING

Floor Beam Specimen Design

As shown in Figure 4, test specimens consisted of a hot-rolled, W8×28 [50 ksi (345 MPa) yield strength per ASTM A992/A992M (2020)] that supported 2.5 in. (64 mm) of lightweight concrete (LWC) on a 2 in. (51 mm) deep galvanized, fluted metal deck [0.037 in. (0.9 mm) thick]. The steel beams were cut to a total length of 163 in. (4.14 m), and the ends were capped with welded steel plates [12 in. × 8 in. × 0.38 in. (305 mm × 203 mm × 9.7 mm)]. The beam ends were positioned on steel angle bearing supports as shown in Figure 4, leaving a clear span of 154.75 in. (3.93 m). The slab had a total width of 47 in. (1.19 m), and the flutes were oriented perpendicular to the beam span. The LWC had a nominal dry density of 115 pcf (1840 kg/m^3) and a specified minimum compressive strength of 3 ksi (20.7 MPa). A single layer of 6×6 W1.4×W1.4 welded wire reinforcement (WWR) [65 ksi (450 MPa) yield strength per ASTM A1064 (2022)] was placed at mid-thickness of the 2.5 in. concrete topping. The slabs were cured for ~8 months prior to testing, and the relative humidity of the concrete was measured to be less than 70% on the day of testing per ASTM E119 (2019).

Table 2. Summary of Previous Quasi-Standard Fire Tests on One-Way Floor Beam Assemblies

Source	Span	Specimen Design	End Conditions	Protection	Fire Exposure	Initial M/Mn	Flexural Failure Criteria
Bletzacker (1967)	16.8 ft (5.12 m)	Beam: 12W×27 Slab: 4 in. (102 mm) flat slab Fully composite (2 tests), Noncomposite (10 tests)	Unrestrained (3 tests), various restraint levels (9 tests)	⅞ in. (22 mm) SFRM on the beam, ½ in. (13 mm) on underside of deck (1.5–2.5 hr rating)	ASTM E119	Constant for each test at 41–60%	"…when the assembly could no longer sustain the vertical design load."
Zhao and Kruppa[a] (1997)	16 ft (4.88 m)	Beam: IPE300 (roughly W12×22) Slab: 4.7 in. (119 mm) flat slab Fully composite (4 tests)	Simply supported beam with unrestrained slab	Unprotected (1 test); 1 in. (25 mm) mineral wool on the beam (3 tests)	ISO 834	Constant for each test at 26–72%	Midspan concrete crushing (3 tests); midspan yielding of steel section (1 test)
Wang et al. (2017)	17.3 ft (5.27 m)	Beam: Built-up (roughly W12×26) Slab: 3.9 in. (99 mm) flat slab Fully composite (1 test), 50% composite (1 test)	Simply supported beam with unrestrained slab	0.43 in. (11 mm) SFRM on the beam	ISO 834	Constant for each test at 50–57%	Maximum deflection of $L/30$
Jiang et al. Test SB2 (2017)	16.7 ft (5.09 m)	Beam: Built-up (roughly W12×26) Slab: 3.9 in. on 3 in. (99 mm on 76 mm) profiled deck Fully composite (1 test)	Simply supported beam with unrestrained slab	0.39 in. (10 mm) SFRM on the beam	ISO 834	Constant at 80%	Maximum deflection of $L/20$
Kordosky et al. (2020)	11 ft (3.35 m)	Beam: W12×26 Slab: 3.25 in. on 2 in. (83 mm on 51 mm) profiled deck 24% composite (2 tests)	Partially restrained simple connection with unrestrained slab	Unprotected (1 test); 2 hr rated SFRM on the beam (1 test); connections protected for both	ASTM E119	Constant for each test at 32%	Maximum deflection of $L^2/(400d)$ and maximum deflection rate of $L^2/(9000d)$
Choe et al.[b] (2020)	40 ft (12.2 m)	Beam: W18×35 Slab: 3.25 in. on 3 in (83 mm on 76-mm) profiled deck 82% composite (4 tests)	Restrained simple connections with slab restrained (2 tests) or unrestrained (2 tests)	SFRM at 2 hr rating on the beam, 3 hr rating on the connections	Parametric fire that initially emulated ASTM E119[c]	Constant for each test at 45%	Maximum deflection of $L/20$

[a] Zhao and Kruppa (1997) Test 5 was partially composite but was halted prematurely due to loading equipment failure; it is therefore excluded.

[b] Choe et al (2020) Test CB-DA was automatically unloaded prior to reaching significant displacement or a collapse state; it is therefore excluded.

[c] Constant 3791 Btu/s (4000 kW) heat release rate was targeted—actual temperatures were 266°F (130°C) hotter than ASTM E119 beyond 15 min.

For the eight noncomposite specimens, a single puddle weld was made in every deck flute to the top flange. The nominal ambient plastic moment strength, M_n, of the noncomposite specimen was, therefore, 1,360 kip-in. (153.7 kN-m), which accounts for the contributions of the steel beam only. For the eight composite specimens, a cluster of four shear studs [each ¾ in. (19 mm) in diameter and 3.5 in. (90 mm) in length] were welded through each deck flute [see Figures 5(b) and 5(c)] to the top flange at 12 in. (305 mm) on longitudinal centers, resulting in a fully composite design per the 2010 AISC *Specification* (AISC, 2010; Vinnakota et al., 1988). The nominal moment strength, M_n, of the composite specimens was calculated to be 2,540 kip-in. (287 kN-m) based on an effective slab width of 39.7 in. (1010 mm) (neglecting contributions from the WWR). The W8×28 section is compact at ambient conditions, and the top flange is assumed to have continuous bracing from the slab.

As shown in Figure 5(a), a gap of 1.5 in. (38 mm) was left between the furnace's restraining support and the welded end plate of each specimen. For the restrained configuration in Figure 5(b), the fluted deck was positioned such that concrete would be placed directly against the furnace support. Also, a groove was cut into the deck so that wet concrete would infill the gap between the beam's end plate and the furnace support. This configuration thus provided full bearing restraint to both the beam and slab against outward thrust from thermal expansion and rotation, though

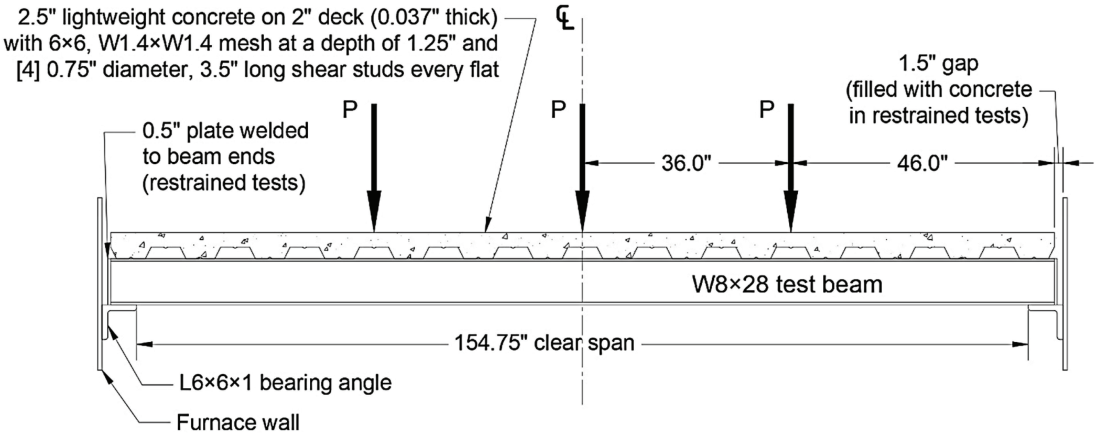

Fig. 4. Side view schematic of the floor beam test specimen, support conditions, and applied loading.

(a) Typical cap-plated beam end prior to deck installation

(b) Restrained configuration

(c) Unrestrained configuration

Fig. 5. Plan-view photos of the beam end conditions before concrete placement (provided by Farid Alfawakhiri, courtesy of AISC).

no restraint would be provided if the specimen were to pull away from the furnace support. For the unrestrained configuration in Figure 5(c), the deck was trimmed such that the concrete placement would stop short of the furnace wall, with a wood rail used to set the unrestrained edge of the slab. Fiberglass fill was placed into gap between the beam's end plate and the furnace support during concrete placement to prevent accidental infill. Both the wood rail and fiberglass fill were removed prior to testing, preserving the gap and allowing unrestrained expansion and rotation at the ends of the beam and slab.

As shown in Figure 6(a), lightweight SFRM with a nominal dry density of 15 pcf (240 kg/m^3) was applied to the steel beams at a uniform thickness of 1 in. (25 mm). The gap between the top flange and underside of the deck between flutes was also filled with SFRM, as is common practice. No other SFRM was applied to the underside of the fluted deck other than some minor overspray just beyond the edges of the top flange. It should be noted that this SFRM application did not formally target a UL-listed assembly hourly rating and was applied solely to enable comparison between test specimens on the basis of their parametric variation.

Test Setup and Loading

Four specimens were simultaneously tested at a time, side-by-side, in the same furnace using the same heat exposure. As shown in Figure 6(b), the unbonded interface between the longitudinal slab edges of neighboring specimens were covered from above with ceramic wool blankets to mitigate the escape of heat during testing. Prior to SFRM application, four thermocouples were installed on the steel beam cross section per the pattern in Figure 1 at four equally spaced locations along its length (for a total of 16 thermocouples per beam). Additional thermocouples were placed throughout the furnace to monitor its internal temperature as well as the temperature increase of the slab at a few locations on the top and bottom surfaces and within. The average of those thermocouples for the R-C test group is plotted in Figure 2 and closely follows the ASTM E119 standard fire curve. The average furnace temperature for all other test groups were similarly consistent with the ASTM E119 fire curve and are not plotted for brevity.

Constant flexural loading beyond the specimen self-weight was applied to each beam using concentrated forces at the three locations in Figure 4 via hydraulic cylinders and bearing plates as shown in Figure 6(b). Each of the four specimens in a simultaneous furnace environment was loaded such that the maximum moment at midspan would reach a different percentage of M_n, ranging from 23 to 60% (see Table 3). These moment calculations assumed simple end supports (since significant rotational restraint would not occur at the beam ends under pure flexural loading at ambient conditions) and an effective span length of 159 in. (i.e., the average of the 163 in. total length and the 154¾ in. clear span). It should be noted that the 57 to 60% flexural utilization level was referred to as the "100% load intensity" by the AISC test team (Alfawakhiri et al., 2016) since it represented a maximum expected or service load condition per ASTM E119 (2019) and allowable strength design per the AISC *Specification* (2022). For simplicity, tests herein are labeled using the following nomenclature: restrained or unrestrained (R/U), composite or noncomposite (C/NC), and initial flexural utilization percentage. For example, R-C-60 refers to the restrained, composite beam tested at an initial ambient flexural utilization of 60%.

(a) Typical SFRM-protected beam (showing the longitudinal seam between slabs of adjacent specimens)

(b) Load application

Fig. 6. Pre-test photos of the experimental setup (provided by Farid Alfawakhiri, courtesy of AISC).

Table 3. Summary of Flexural Loading and Corresponding Critical Temperatures per Load-Dependent Relationships in the AISC *Specification* (2022) and Eurocodes 3 and 4 (CEN, 2005, 2008)

Initial Flexural Utilization, M/M_n		Load P [kips (kN)]	$T_{cr,BF}$ [°F (°C)]		T_{cr} [°F (°C)]	
			AISC *Specification* Table A-4.2.4	EC4 Part 1-2, Section 4.3.4.2.3(4)	AISC *Specification* Equation A-4-23	EC3 Part 1-2, Equation 4.22
Composite	60%	17.8 (79.2)	1100 (593)	1030 (554)	972 (522)	1030 (554)
	48%	14.1 (62.7)	1209 (654)	1096 (591)	1041 (560)	1096 (591)
	36%	10.5 (46.7)	1313 (712)	1177 (636)	1129 (609)	1177 (636)
	24%	6.82 (30.3)	1429 (776)	1288 (698)	1253 (678)	1288 (698)
Noncomposite	57%	8.75 (38.9)	1130 (610)	1047 (564)	990 (532)	1047 (564)
	45%	6.90 (30.7)	1232 (667)	1113 (600)	1058 (570)	1113 (600)
	34%	5.05 (22.5)	1331 (721)	1193 (645)	1146 (619)	1193 (645)
	23%	3.20 (14.2)	1448 (787)	1303 (706)	1270 (688)	1303 (706)

Before any heat was applied, simultaneous testing for four side-by-side specimens was initiated by slowly applying all loads for several minutes until equilibrium was achieved. Heating via the ASTM E119 standard fire curve was then initiated, and the loading was held constant until the specimen was deemed to be no longer capable of sustaining the applied loads. Generally, this meant that the midspan deflection had surpassed the corresponding ASTM E119 criteria per Table 1:

- Composite beam:
  - Deflection limit = $L^2/[400(d_{beam}+d_{slab})]$ = 4.81 in. (122 mm)
  - Deflection rate limit = $L^2/[9000(d_{beam}+d_{slab})]$ = 0.214 in/min (5.44 mm/min)
- Noncomposite beam:
  - Deflection limit = $L^2/(400d_{beam})$ = 7.51 in. (191 mm)
  - Deflection rate limit = $L^2/(9000d_{beam})$ = 0.334 in/min (8.48 mm/min)

Upon reaching these limits, the applied loading for that specimen would be removed, although active heating would continue until all four specimens reached the deflection limit states. The midspan deflection of each beam was measured as the increase in distance between the top-of-slab and the underside of the overhead loading frame. These measurements were initiated after the beam was fully loaded and before heating was applied, such that the small amount of deflection in the loading frame due to the reactions from load application would be neglected.

Thermal Response

The temperatures measured in the flanges and web of the four steel beams with the highest loading percentages are plotted in Figure 7 for demonstration—all other specimens with lower loading have very similar steel temperature time histories as those shown here and are thus not provided for brevity. The solid "Avg" curves for $T_{s,TF}$, $T_{s,BF}$, and $T_{s,web}$ represent the mean value of all thermocouples on a corresponding plate over the length of the beam. The dashed curves represent the maximum and minimum recorded temperatures at any single thermocouple on that plate over the length of the beam. The average temperature in each plate is very consistent between specimens. The bottom flange experiences the greatest temperature increase due to its large amount of fire-exposed surface. The web also has a significant amount of exposed surface and is thinner than the flanges, and it therefore develops temperatures that are up to ~200°F (93.3°C) lower than the bottom flange. The difference between maximum and minimum recorded temperature for the bottom flange and web typically does not exceed ~100°F (37.8°C) because they are more uniformly heated. The top flange has a greater range between its minimum and maximum value and develops a lower average temperature because it is in contact with the slab and has less surface area exposed to fire. The top surface of the top flange conducts heat to the slab, which has significant thermal mass and remains cooler than the steel beam throughout the test. Note that the thermal transmission through the slab is not considered to be within the scope of this paper and is therefore not presented; the reader is instead referred to the paper by Alfawakhiri et al. (2016) for that information.

The time at which each specimen reached flexural runaway is also marked in each plot in Figure 7. The temperature time history for U-NC-57 in Figure 7(d) shows a sudden increase in $T_{s,TF}$ at this point, indicating that the SFRM on that plate began to delaminate when the beam lost its flexural resistance. In particular, the maximum temperature for $T_{s,TF}$ converges to the fire curve near the end of the heat application around ~160 min. As will be shown in the next section, U-NC-57 experienced the largest deflection among the four specimens plotted here, which likely enabled the SFRM delamination. It should be noted that U-NC-45 and U-NC-34 also showed similar signs of top flange SFRM delamination at the onset of flexural runaway but at a later time due to their lower level of loading. The $T_{s,TF}$ curve for R-NC-57 in Figure 7(c) also shows indications of minor SFRM delamination (via a sudden uptick in maximum $T_{s,TF}$) but not until 30 min after the loss of flexural resistance. The $T_{s,TF}$ curve of the other R-NC specimens did not show any noticeable signs of SFRM delamination. Likewise, the steel temperature curves for the composite specimens in Figure 7(a-b) are relatively smooth throughout heating and also indicate no obvious disruption to the integrity of the SFRM.

Figure 8 shows good overall consistency among all 16 specimens regarding their average values of $T_{s,BF}$ and $T_{s,E119}$, calculated across all pertinent thermocouple locations for each specimen. The curves for $T_{s,BF}$ in Figure 8(a) are especially consistent due to the preservation of SFRM integrity on the bottom flange throughout heating, even past the onset of flexural runaway. Due to late onset of SFRM delamination from the top flange, the three gray curves for $T_{s,E119}$ in Figure 8(b) from U-NC specimens with 57%, 45%, and 34% flexural utilization trend higher beyond 120 min than those for all other specimens.

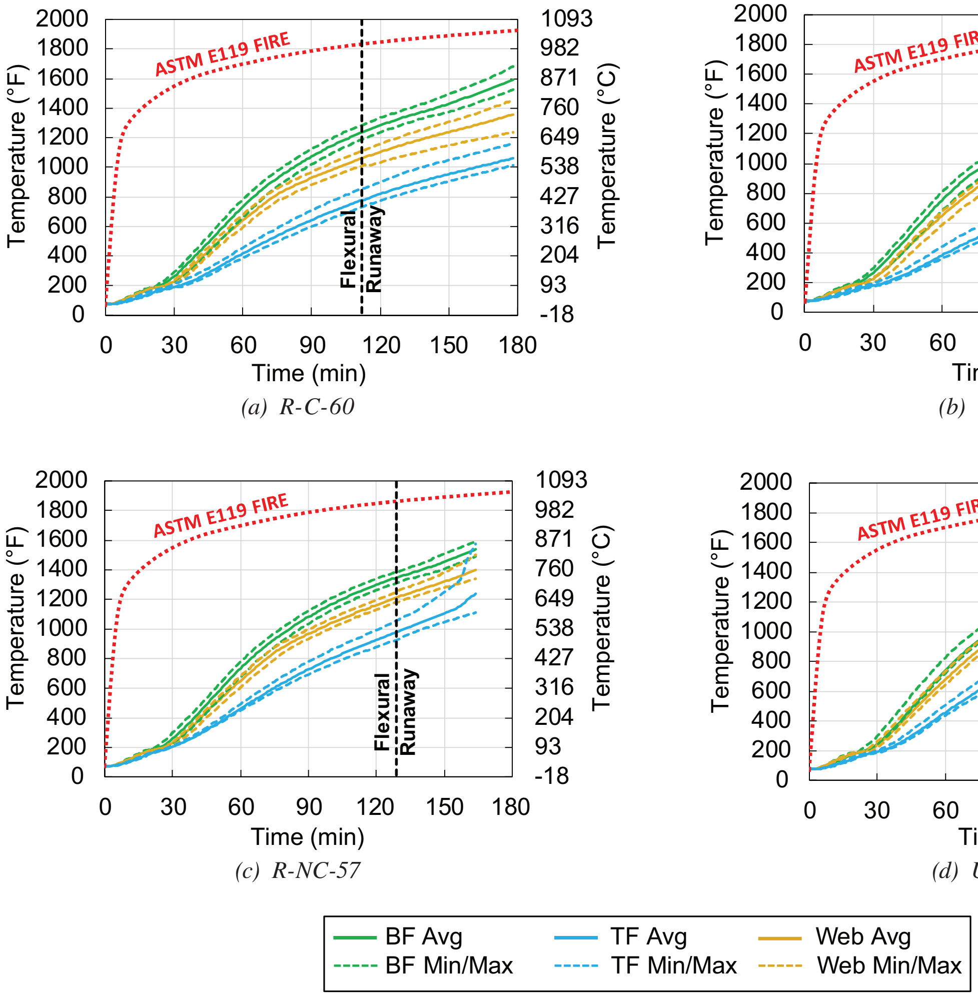

(a) R-C-60

(b) U-C-60

(c) R-NC-57

(d) U-NC-57

Fig. 7. Measured time histories of $T_{s,BF}$, $T_{s,web}$, *and* $T_{s,TF}$ *for indicated specimens (experimental data provided by Farid Alfawakhiri, courtesy of AISC).*

Flexural Response

The measured time histories of vertical midspan deflection for all 16 tests are plotted in Figure 9, with the ASTM E119 criteria from Table 1 implemented as follows:

- The corresponding ASTM E119 deflection limits for composite and noncomposite specimens are marked as a dashed horizontal line in Figure 9, while an “×” is used to mark the time at which the deflection rate limit is met. Eleven of the 16 specimens met both criteria;

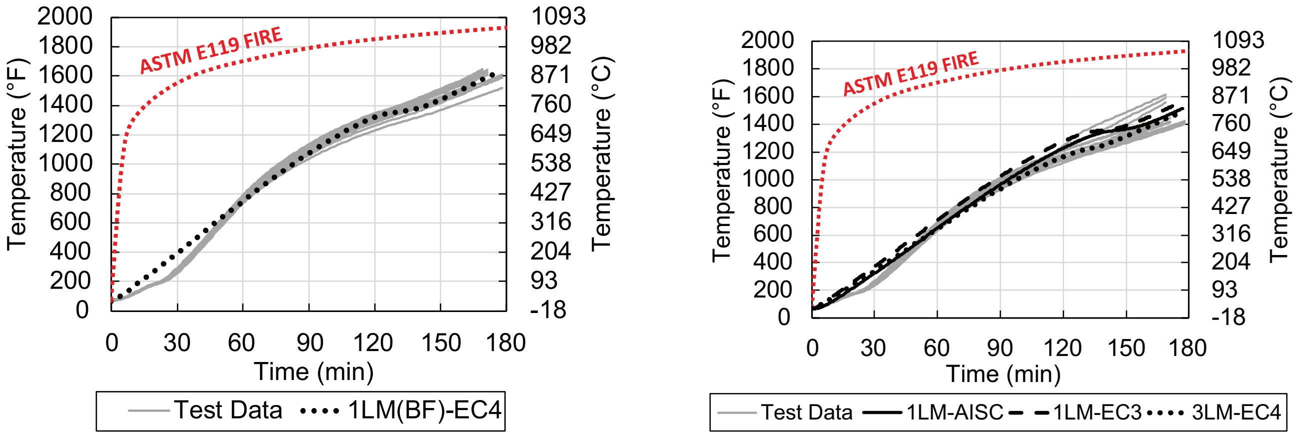

(a) $T_{s,BF}$ *(b)* $T_{s,E119}$

Fig. 8. Comparison of steel temperature time histories from all 16 test specimens (calculated as an average of all longitudinal measurement locations on each beam) against lumped mass temperature predictions (experimental data provided by Farid Alfawakhiri, courtesy of AISC).

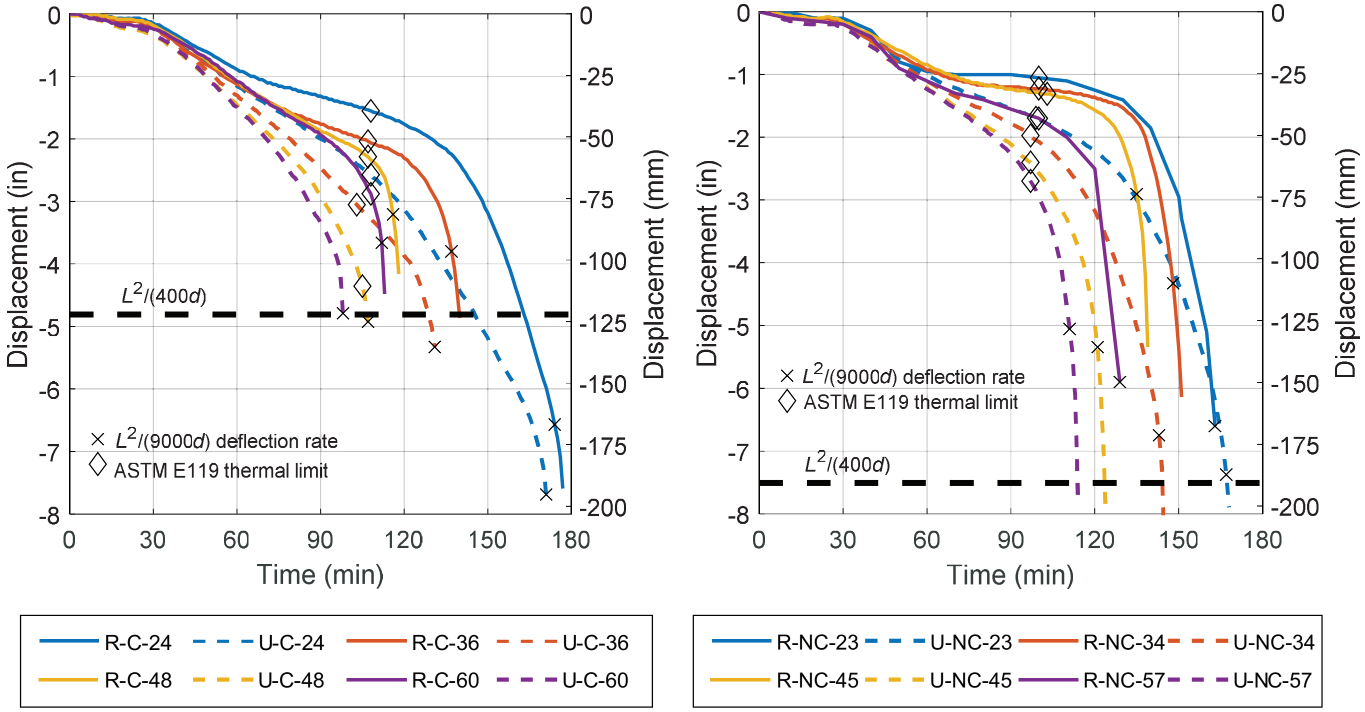

(a) Composite *(b) Noncomposite*

Fig. 9. Measured time histories of vertical midspan deflection for standard fire test specimens (experimental data provided by Farid Alfawakhiri, courtesy of AISC).

restrained specimens R-C-60, R-C-48, R-NC-57, R-NC-45, and R-NC-34 exceeded the deflection rate, but these tests were stopped before reaching the deflection limit to protect the testing equipment from the rapid onset of runaway deflection. The end result for these specimens was deemed to sufficiently signify the loss of flexural resistance.

- The time at which the ASTM E119 thermal limits for $T_{s,MAX}$ or $T_{s,E119}$, whichever came first, are exceeded is marked with a diamond on each curve in Figure 9. The temperatures used to calculate the limits are reflected in the gray curves in Figure 8. All specimens in this test program were governed by the average temperature criteria, $T_{s,E119}$. $T_{s,MAX}$ was typically exceeded in the bottom flange 5–10 min later than $T_{s,E119}$.

The ASTM E119 thermal limit was reached for all specimens between 100 and 110 min, and Figure 9 shows that this flat threshold does not adequately describe the loss of flexural resistance when variations in applied loading are considered. In fact, U-C-60 was the first specimen to exceed both deflection criteria at ~95 min, even though its T_{E119} was still ~50°F (28°C) lower than the corresponding thermal limit. R-C-24 reached flexural runaway just past 175 min, roughly 1 hr after the thermal limit was exceeded. The time needed to reach the thermal and structural limits generally showed closer agreement at higher flexural utilizations, but the deflection limits were reached at significantly longer times when flexural utilization was reduced.

As expected, the restrained specimens exhibited a stiffer initial flexural resistance response in Figure 9 than their unrestrained counterparts at equivalent loads and, as a result, achieved slightly longer times to flexural runaway. All specimens show relatively similar initial deflection down to a value of ~1 in., after which the deflection rate for restrained specimens becomes shallower due to the growing influence of restraint forces and hogging moment at the beam ends. After they have stiffened and developed additional restraining stresses, however, the restrained specimens then develop a rapid increase in deflection rate toward runaway failure at lower magnitudes of deflection than in the unrestrained cases. The unrestrained specimens exhibit a more gradual overall deflection response as their temperatures increases, with the deflection rate accelerating toward runaway only in the last few minutes before the loading was stopped.

Observations from Post-Test Inspection

Photos from the post-fire inspection of each group of specimens are shown in Figures 10 and 11. Photos taken from above show that all four specimens in each group exhibited similar ultimate deflected shapes regardless of initial flexural utilization, even though flexural resistance was exceeded at different times according to the applied load level. Figures 10(a) and 11(a) clearly show that the hogging moment at the ends of the restrained specimens caused significant transverse cracking in the top of the composite slab [Figure 10(b)] as well as plastic hinging at the end of the beam [Figures 10(c) and 11(b)]. Despite lacking a true connection, the restrained specimens were able to develop these hogging moments at their ends due to the compressive reaction of the end plates against the furnace supports to resist axial thermal expansion. As shown previously in Figure 7, the bottom flange and web undergo a larger temperature increase and would therefore experience more restraint of thermal expansion than the top flange and slab. Larger horizontal compressive reactions near the bottom of the beam would produce an eccentricity at the contact of the end plate against the support, thereby inducing the hogging moment (i.e., inducing upward rotation) that is observed at the ends of the restrained specimens.

For the unrestrained specimens in Figures 10(d) and 11(c), the gap between the furnace support and the ends of the specimens allowed thermal expansion and end rotation; therefore, there was no noticeable post-test transverse cracking or plastic hinging near the unrestrained ends. The final parabolic deflected shapes of the unrestrained specimens in Figures 10(f) and 11(d) resemble the anticipated deflected shapes for idealized simply supported boundary conditions intended by the standard test setup. The U-NC specimens in Figure 11(c) show very little slab cracking due to the relatively low engagement of the noncomposite slab; however, increased deflections due to lower stiffness caused some observable SFRM delamination, particularly at the top flange [see Figure 11(d)]. This observation supports the onset of rapid temperature increase in the top flange after flexural runaway as shown previously for U-NC-57 in Figure 7(d). Conversely, Figures 10(c) and 10(f) show that none of the composite beam specimens experienced noticeable SFRM loss prior to the loss of flexural resistance.

As shown in Figure 10(e), the U-C specimens developed large lengthwise longitudinal cracks just beyond the width of the bearing plates for point load application. No transverse support was provided to the slab edges in these tests, and it should be noted that longitudinal cracking would not be expected in an actual building with a continuous slab that spanned transversely to the next parallel floor beam. In these tests, the longitudinal cracking of the U-C specimens was likely caused by differential thermal expansion between the beam and unrestrained composite slab (which was significantly cooler than the beam due to its larger thermal mass, lower thermal conductivity, and lower ratio of heated area to overall volume). The hotter beam is, therefore, longitudinally restrained by the cooler slab due to their composite interface. The unrestrained slab, as a result, develops nonuniform transverse stress distribution, and the

(a) R-C specimens from above *(d) U-C specimens from above*

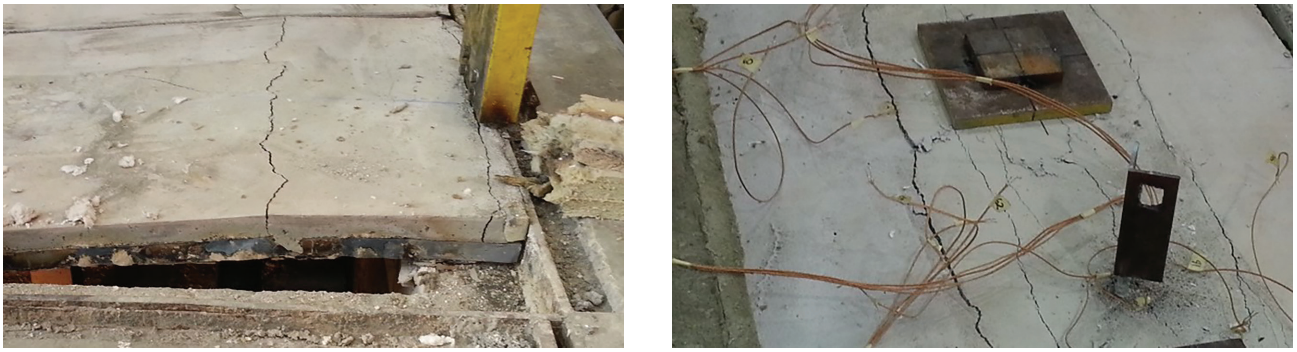

(b) R-C slab edge transverse cracking *(e) U-C longitudinal slab cracking*

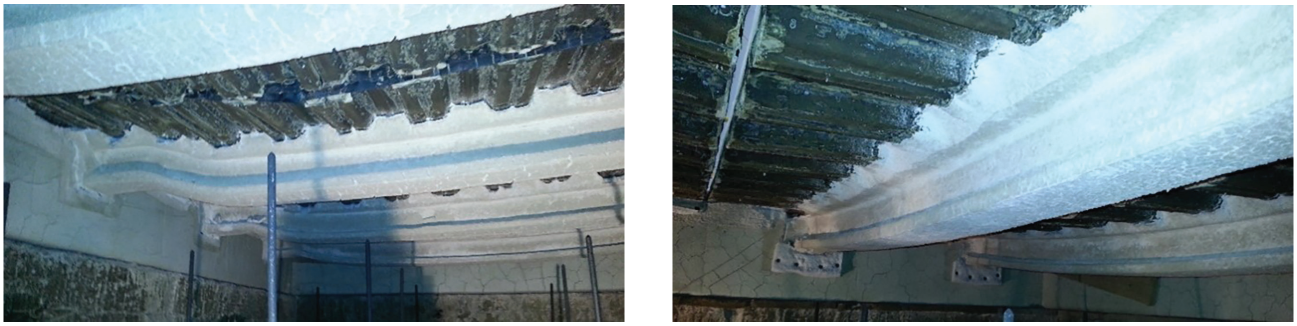

(c) R-C specimens from below *(f) U-C specimens from below*

Fig. 10. Post-test photos of the composite specimens (provided by Farid Alfawakhiri, courtesy of AISC).

longitudinal cracks indicate a shear plane in the transition between the highly composite center portion and the less restrained outer portions of the slab.

Critical Temperature Verification

The plots in Figure 12 are similar to those in Figure 3, but the data points from previous experimental studies have been replaced with those derived from the standard fire tests of the 16 specimens. The following critical temperatures are taken for each specimen at the time at which the specimen reached the ASTM E119 deflection rate limit (again, marked with an "×" in Figure 9): (a) maximum $T_{s,BF}$ measured at any location along the length of the beam and (b) maximum $T_{s,E119}$ at any one of the three cross-section locations along the length of the beam, as shown in Figure 1(b). Both plots again show that the ASTM E119 flat critical temperature limits do not accurately capture the effects of applied loading on structural resistance to standard fire exposure. The best correlation for those limits is observed at 48% initial flexural utilization, which is consistent with the fact that the 1100°F (593°C) critical temperature limit for $T_{s,E119}$ correlates to an approximate 50% reduction in steel yield strength (AISC, 2022; CEN, 2005). The AISC *Specification* flexural retention factor provides a conservative lower bound across all critical $T_{s,BF}$ in Figure 12(a). AISC *Specification* Equation A-4-23 (Equation 1) and the Eurocode critical temperature per Equation 2 (which are intended to represent the temperature of the entire steel member) logically provide a closer correlation to critical $T_{s,E119}$ across all tests in Figure 12(b) but provide an unnecessarily conservative prediction of critical $T_{s,BF}$ in Figure 12(a).

It should be noted that the noncomposite specimens consistently exhibited ~100°F (37.8°C) higher critical temperature at the onset of flexural runaway than their composite

(a) R-NC specimens from above

(c) U-NC specimens from above

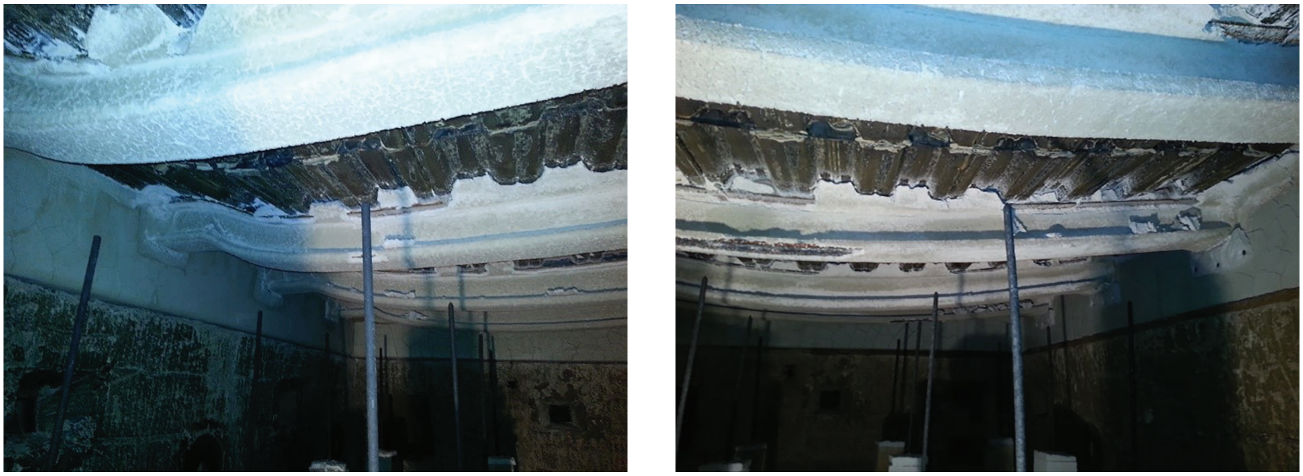

(b) R-NC specimens from below

(d) U-NC specimens from below

Fig. 11. Post-test photos of the noncomposite specimens (provided by Farid Alfawakhiri, courtesy of AISC).

Table 4. Summary of Standard Fire Resistance Times (in minutes) Based on Thermal and Structural Test Results

Initial Flexural Utilization, M/M_n		Limit: ASTM E119 Deflection Rate		Limit: AISC $T_{cr,BF}$		Limit: AISC T_{cr}	
		R-Test Deflection	U-Test Deflection	R-Test $T_{s,BF}$	U-Test $T_{s,BF}$	R-Test $T_{s,E119}$	U-Test $T_{s,E119}$
Composite	60%	112	98	93	89	96	93
	48%	116	107	104	100	101	101
	36%	137	131	123	116	118	115
	24%	174	171	161	141	144	140
Noncomposite	57%	129	114	95	92	93	90
	45%	139	123	104	102	99	96
	34%	151	144	124	117	114	108
	23%	163	167	154	139	138	132

counterparts. It is likely that the noncomposite slab made a non-negligible contribution to the flexural resistance of those beams; however, the loading applied to each noncomposite beam was calculated as a percentage of the beam's plastic moment capacity only. Excess capacity relative to the assumed level of initial flexural utilization would therefore translate into a higher critical temperature at the onset of flexural runaway. This design concept indicates that the design flexural utilization (as plotted) is often a conservative estimate of noncomposite strength, meaning that critical temperature relationships as a function of flexural utilization for composite beams can be used to conservatively estimate noncomposite critical temperature relationships.

Table 4 summarizes the times at which each specimen reached the ASTM E119 deflection rate limit. Also shown are the times at which the recorded average $T_{s,BF}$ and $T_{s,E119}$ from each specimen (plotted previously in Figure 8) reach their corresponding AISC critical temperature from Table 3. The relationship between these fire resistance times is visualized in Figure 13 as a correlation plot, with thermally predicted values on the vertical axis and deflection-based values on the horizontal axis. Points that fall below the 1:1 line indicate that the thermal prediction of fire resistance is lower (or conservative) relative to the deflection-based resistance. The banded lines indicate a percentage of increase or decrease in thermally predicted fire resistance versus the deflection-based resistance.

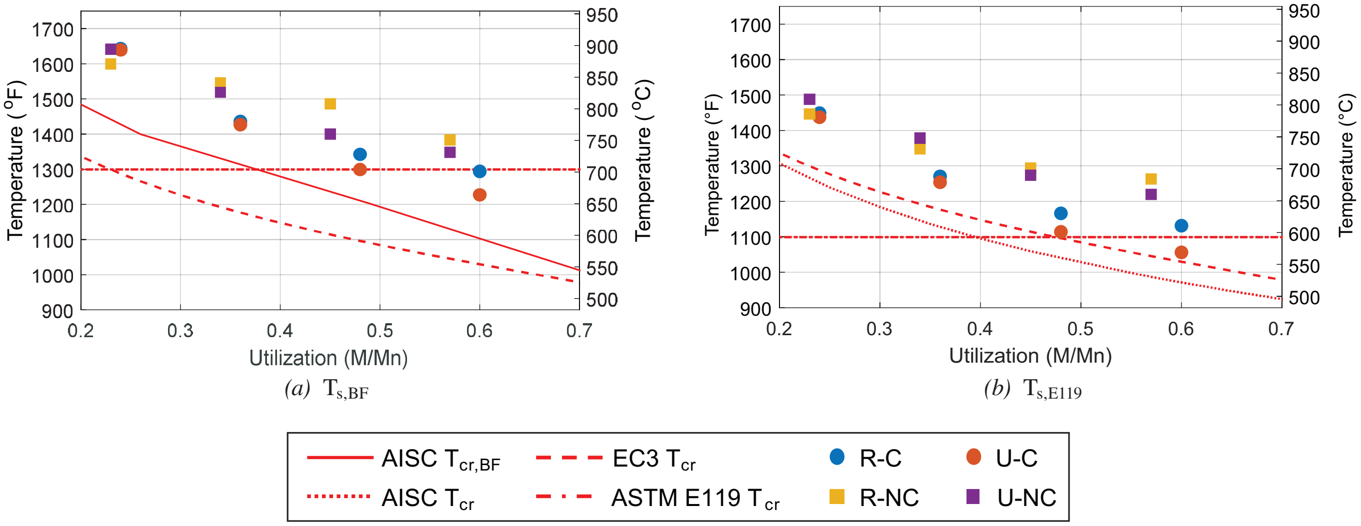

(a) $T_{s,BF}$

(b) $T_{s,E119}$

Fig. 12. Critical steel temperatures for flexural failure of standard fire test specimens as a function of initial ambient flexural utilization.

Figure 13 shows that imposing the AISC *Specification* critical temperature limits on the experimental measurements of $T_{s,BF}$ and $T_{s,E119}$ provides similarly conservative fire resistance predictions relative to the onset of flexural runaway. Fire resistances based on critical temperatures for noncomposite specimens are more conservative, again because the calculation of initial flexural utilization neglected any flexural contributions from the slab. Fire resistance times based on critical temperatures for the composite specimens show good agreement with flexural runaway (with most no more than 15% conservative), while those for noncomposite specimens are 15–30% conservative. As shown in Figure 12(b), the Eurocode 3 critical temperatures are slightly greater than the AISC *Specification* Equation A-4-23 curve and would, therefore, be expected to provide even closer predictions of flexural runaway under standard fire exposure when used with $T_{s,E119}$. Altogether, these results suggest that these critical temperature limits can provide reasonably conservative estimates of one-way flexural resistance to standard fire exposure for this type of floor beam assembly.

SIMPLIFIED METHODS FOR CRITICAL TEMPERATURE ANALYSIS

There are currently no provisions in the AISC *Specification* for determining critical temperature per Section A-4.2.4e for floor beams. Also, there are no direct means per Section A-4.3.1 for achieving equivalence to a standard fire resistance rating other than through an advanced analysis method outlined in Section A-4.2.4c. Typically, this analysis would use a 2D or 3D finite element (FE) mesh (Drury and Quiel, 2023b; Franssen and Gernay, 2017; Selden and Varma, 2016) of the composite or noncomposite beam cross section. Rather than resorting to such advanced analysis methods (which require greater effort and expertise by the analyst), the temperature increase in a protected W-shape floor beam cross section can instead be predicted using lumped mass (LM) thermal analysis techniques, which are classified as simple analysis methods in Section A-4.2.4d. The W-shape beam section can be represented as a single LM (AISC, 2022; Buchanan and Abu, 2017; CEN, 2005; Gamble, 1989), or multiple LMs can be used to represent the flange and web plates (CEN, 2008; Drury et al., 2020, 2021; Ghojel and Wong, 2005). These methods can be implemented in spreadsheets or other simple mathematical solvers and have been shown to provide conservatively accurate predictions of thermal behavior in experimental testing of composite floor beams (Drury et al., 2020, 2021; Drury and Quiel, 2023b). The simplified LM calculations presented herein are demonstrated as capable tools for predicting critical temperature for floor beams while simultaneously providing a means of calculating equivalence to ASTM E119 hourly fire resistance ratings.

Single Lumped Mass Methods

The following calculations from the AISC *Specification* and Part 1-2 of Eurocode 3 represent the steel beam section as a single lumped mass (1LM) that has uniform temperature

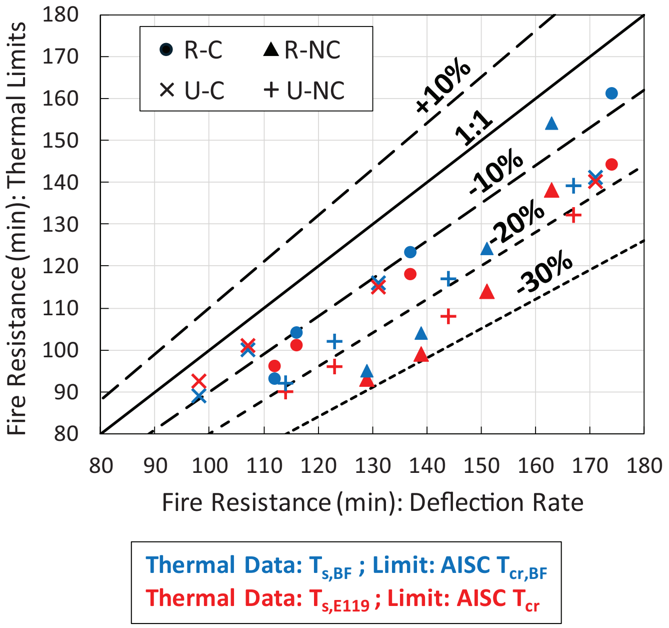

Fig. 13. Correlation plot of standard fire resistance times based on thermal and structural test results.

T_s and is uniformly coated with a contoured constant thickness of fire protective insulation:

AISC *Specification* Equation C-A-4-7 (U.S. units):

$$T_{s,i} = T_{s,i-1} + \frac{k_{p,i}}{d_p}\left[\frac{T_{f,i} - T_{s,i-1}}{c_{s,i}\left(\dfrac{W}{D}\right) + \dfrac{c_{p,i}\rho_{p,i}d_p}{2(144)}}\right]\Delta t \tag{3}$$

Eurocode 3, Part 1-2, Equation 4.27 (metric units):

$$T_{s,i} = T_{s,i-1} + \frac{k_{p,i}}{d_p}\left[\frac{T_{f,i} - T_{s,i-1}}{c_{s,i}\left(\dfrac{W}{D}\right) + \dfrac{c_{p,i}\rho_{p,i}d_p}{3}}\right]\Delta t \tag{4a}$$

$$-\left(e^{\phi_i/10} - 1\right)\left(T_{f,i} - T_{f,i-1}\right)$$

$$\phi_i = \frac{c_{p,i}\rho_{p,i}d_p}{c_{s,i}\left(\dfrac{W}{D}\right)} \tag{4b}$$

where

A_s = total cross-sectional steel area, ft^2 (m^2)

D = heated perimeter, in. (mm)

$T_{f,i}$ = temperature of the fire at time step i, °F (°C)

$T_{s,i}$ = temperature of the steel section at time step i, °F (°C)

W = weight (mass) per unit length, lb/ft (kg/m) = $\rho_s A_s$

$\dfrac{W}{D}$ = section factor for the fire exposed surfaces

$c_{s,i}$ = steel specific heat at time step i, Btu/lb-°F (J/kg-K)

$c_{p,i}$ = fire protection specific heat at time step i, Btu/lb-°F (J/kg-K)

d_p = fire protection thickness, in. (m)

i = time step number

$k_{p,i}$ = fire protection thermal conductivity at time step i, Btu/ft-sec-°F (W/m-K)

Δt = time step increment (sec)

$\rho_{p,i}$ = fire protection density at time step i, lb/ft^3 (kg/m^3)

ρ_s = steel density = 490 lb/ft^3 (7,850 kg/m^3)

Note that the original form of Equation 4 from Eurocode 3 has been reformatted to be similar to Equation 3 (which is taken from the AISC *Specification)* to facilitate a direct comparison. The two 1LM calculation approaches are similarly based on the assumption that the outer surface of the protection layer is equal to the fire temperature, and the inner surface of the protection layer is equal to the steel temperature. Eurocode includes an additional reduction in $\Delta T_{s,i}$ at every time step as a function of the change in applied fire temperature $\Delta T_{f,i}$ during that step. In this way, the Eurocode formulation slightly reduces $\Delta T_{s,i}$ when the fire temperature is growing at a rapid rate.

The value of D for both formulations is calculated using the inner perimeter of the contoured fire protection per Eurocode 3 (CEN, 2005). For a W-shape floor beam section that supports a slab, D is calculated as follows:

$$D = 2d + 3b_f - 2t_w \tag{5}$$

In this study, the thermal properties of the steel and SFRM are realistically considered as a function of their increasing temperature. To avoid the need for iteration at each time step, these properties can be calculated using temperatures obtained at the previous time step (Drury et al., 2020; Gamble, 1989), as long as the time step remains sufficiently small. The following calculations are made to obtain the thermal properties of the steel and SFRM at each time step i:

- $c_{s,i}$ for the steel section is calculated as a function of $T_{s,i-1}$ using the temperature-dependent relationship in Eurocode 3, Part 1-2 (CEN, 2005).
- $c_{p,i}$, $k_{p,i}$, and $\rho_{p,i}$ for the fire protection are calculated as a function of the assumed temperature of the fire protection material, $T_{p,i}$, taken as $T_{p,i} = \left(0.9T_{s,i-1} + 0.1T_{f,i-1}\right)$ using the mean value of the empirical relationship per Khorasani et al. (2015) for standard, low-density SFRM (with a density of approximately 15 pcf (240 kg/m^3)].

For this study, all LM thermal calculations are performed using Δt = 30 sec in accordance with Eurocode 3, Part 1-2 (CEN, 2005), which was sufficiently small to obtain convergent solutions as well as good agreement with the experimentally measured $T_{s,E119}$ [see Figure 8(b)]. The use of weighted average $T_{p,i} = \left(0.9T_{s,i-1} + 0.1T_{f,i-1}\right)$ to calculate the temperature-dependent SFRM properties was also determined based on good agreement with the experimental data. The stronger weighting of the steel temperature reflects the presumed shape of the thermal gradient that develops over the thickness of the SFRM when exposed to fire. Specifically, the high temperature at the fire-exposed outer SFRM surface would exhibit an approximately exponential decay over the SFRM thickness toward the protected inner surface of the steel section. More research is needed to demonstrate a broad applicability of this approach for calculating temperature-dependent SFRM thermal properties in these 1LM methods. Figure 8(b) shows that the simpler AISC formulation provides a slightly closer prediction of the experimentally measured $T_{s,E119}$ than the EC3 formulation when using the same material inputs.

Multiple Lumped Mass Method

As shown in Figure 7, the bottom flange, top flange, and web will realistically develop different temperatures due to differences in fire-exposed perimeter; the assumption of a single uniform T_s for the entire cross section is therefore a significant simplification. As an alternative, the steel section can be subdivided into multiple lumped masses for which a thermal calculation can be made at each time step (Drury et al., 2020, 2021; Ghojel and Wong, 2005). Part 1-2 of Eurocode 4 adapts the equations from Part 1-2 of Eurocode 3 such that each flange and the web are considered as separate LMs:

Eurocode 4, Part 1-2, Equation 4.8 (metric units):

$$T_{s,j,i} = T_{s,j,i-1} + \frac{k_{p,j,i}}{d_{p,j}}\left[\frac{T_{f,i} - T_{s,j,i-1}}{c_{s,j,i}\left(\dfrac{W_j}{D_j}\right) + \dfrac{c_{p,j,i}\,\rho_{p,j,i}\,d_{p,j}}{3}}\right]\Delta t - \left(e^{\phi_{j,i}/10} - 1\right)\left(T_{f,i} - T_{f,i-1}\right) \tag{6a}$$

$$\phi_{j,i} = \frac{c_{p,j,i}\,\rho_{p,j,i}\,d_{p,j}}{c_{s,j,i}\left(\dfrac{W_j}{D_j}\right)} \tag{6b}$$

where

j = plate component designation (*BF, TF, web*)

$T_{s,j,i}$ = temperature of plate component j at time step i, °C

$\dfrac{W_j}{D_j}$ = section factor for the fire exposed surfaces of plate component j

In the Eurocode 4 approach, the section factor W_j/D_j for each flange is calculated using the following inputs:

Bottom flange: $$D_{BF} = 2t_f + 2b_f \tag{7a}$$

$$A_{s,BF} = b_f t_f \tag{7b}$$

Top flange: $$D_{TF} = 2t_f + b_f \tag{7c}$$

$$A_{s,TF} = b_f t_f \tag{7d}$$

Again, note that the original form of Equation 6 from Eurocode 4 has been reformatted to be similar to Equation 3 for comparison. Figure 8(a) shows very good agreement between the experimental measurements of $T_{s,BF}$ and that predicted by the Eurocode 4 approach for the *BF* as a single lumped mass (1LM). If the beam depth does not exceed 20 in. (500 mm), Eurocode 4 notes that the temperature of the web can be taken as equal to that of the bottom flange for simplification:

$$T_{s,web,i} \approx T_{s,BF,i} \tag{8}$$

The average temperature of the W-shape cross section can then be calculated as an area-weighted average among the three plate lumped masses (3LM):

$$T_{s,AVG,i} = \sum_{j=1}^{3} T_{s,j,i}\left(\frac{A_{s,j}}{A_s}\right) \tag{9}$$

Figure 8(b) shows that $T_{s,AVG}$ per the 3LM approach in Equation 9 provides an even closer prediction of the experimentally measured $T_{s,E119}$ than the 1LM approaches.

Sensitivity to SFRM Thermal Properties

It should be emphasized that the accuracy of these LM predictions is dependent on the temperature-dependent relationships used to obtain thermal properties of the steel and fire protection materials. For comparison, two additional predictions of T_s are made using Equation 3 from the AISC *Specification* but with two alternative temperatures used to calculate the SFRM thermal properties at every time step via the Khorasani et al. (2015) mean value relationships for $c_{p,i}$, $k_{p,i}$, and $\rho_{p,i}$: $T_{p,i} = 500°\text{C}$ (as permitted by the AISC *Specification* as a simplification), and $T_{p,i} = T_{s,i-1}$ (representing a lower-bound simplification). Figure 14 shows that these alternate approaches can provide predictions of $T_{s,E119}$ that are either slightly higher or lower, respectively, versus the experimental data or the 1LM-AISC prediction of T_s using $T_{p,i} = (0.9T_{s,i-1} + 0.1T_{f,i-1})$ (reproduced from Figure 8). The user should exercise caution and potentially seek opportunities for preliminary experimental validation when applying these methods in practice to calculate equivalent standard fire resistance. Also note that some of the gray curves representing the experimental data begin to

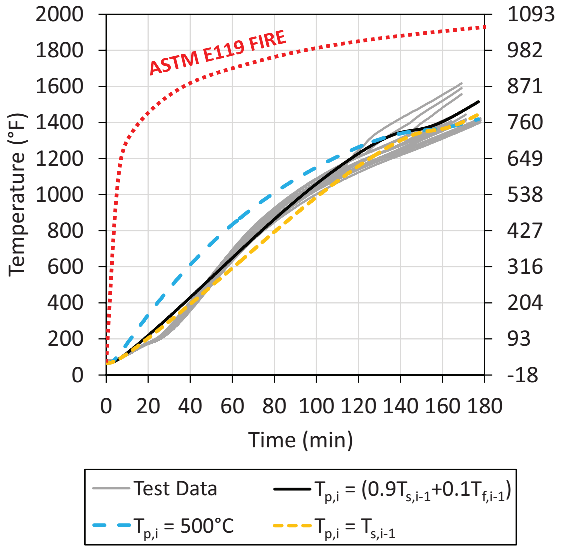

Fig. 14. Comparison of time histories for $T_{s,E119}$ *from all 16 specimens (calculated as an average of all longitudinal measurement locations for each beam) against 3 iterations of the AISC Specification 1LM prediction for* T_s *(with different values of* T_p *used to determine the SFRM thermal properties at each time step) (experimental data provided by Farid Alfawakhiri, courtesy of AISC).*

Table 5. Comparison of Standard Fire Resistance Times (in minutes): Flexural Performance of Tested Specimens Versus Thermal LM Predictions of Load-Dependent Critical Temperature.

Initial Flexural Utilization, M/M_n		Limit: ASTM E119 Deflection Rate		Limit: AISC $T_{cr,BF}$	Limit: AISC T_{cr}	Limit: EC3 T_{cr}	
		R-Test Deflection	U-Test Deflection	1LM EC4 $T_{s,BF}$	1LM AISC T_s	1LM EC3 T_s	3LM EC4 $T_{s,AVG}$
Composite	60%	112	98	93	91	91	101
	48%	116	107	105	98	98	110
	36%	137	131	119	108	107	122
	24%	174	171	149	123	122	146
Noncomposite	57%	129	114	96	93	92	104
	45%	139	123	108	100	100	113
	34%	151	144	122	110	109	125
	23%	163	167	151	126	124	148

trail upward beyond 120 min, due to likely SFRM loss after the onset of flexural runaway.

Critical Temperature Predictions

The load-dependent critical temperature relationships from Table 3 can be applied to the various LM predictions of T_s to predict the standard fire resistance. Table 5 compares these predictions against the fire resistance times corresponding to the onset of flexural runaway in each test (which are reproduced from Table 4). Similar to Figure 13, the relationship between these fire resistance times is visualized in Figure 15 as a correlation plot, with LM thermal predictions on the vertical axis and deflection-based values from the tests on the horizontal axis. Points that fall below the 1:1 line indicate that the LM prediction of fire resistance is lower (or conservative) relative to the deflection-based resistance. Due to the enhanced accuracy of the Eurocode 4 LM predictions of steel temperature (see Figure 8), the predicted fire resistance times based on those calculations (plotted in red and blue in Figure 15) are similarly conservative as those based on the experimentally measured temperatures in Figure 13. Fire resistances based on the 1LM methods (plotted in green and gold in Figure 15) are slightly more conservative than those in Figure 13 because their predictions of T_s are more conservative relative to the experimentally measured T_s (see Figure 8).

CONCLUSIONS

The results of this study demonstrate that simplified thermal analysis methods can be combined with load-dependent critical temperature relationships to conservatively predict the standard fire resistance of W-shape floor beam assemblies at flexural runaway. In practice, a designer would be able to iteratively perform these calculations to determine the thickness and material properties of SFRM needed to achieve an equivalent targeted hourly fire resistance rating

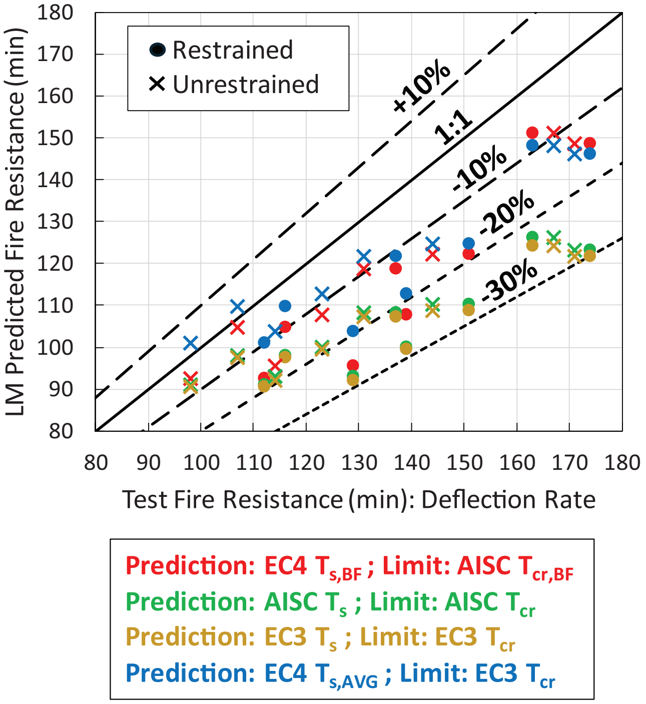

Fig. 15. Correlation plot of standard fire resistance times from structural test results versus thermal LM predictions of load-dependent critical temperature.

for a given floor beam section. The design of floor beams is often governed by deflection-based serviceability criteria rather than strength criteria; the load-dependent critical temperature relationships per the AISC *Specification* and Part 1-2 of Eurocodes 3 and 4 therefore offer the ability to tailor an equivalent standard fire resistance to the actual flexural utilization of the member.

The following conclusions can be drawn from this study:

- Based on the results of standard fire testing by AISC/AISI in 2015 (as well as other quasi-standard fire test results in the published literature), the critical value of bottom flange temperature, $T_{s,BF}$, at the onset of flexural runaway can be conservatively predicted using the load-dependent values of $T_{cr,BF}$ in AISC *Specification* Table A-4.2.4 (2022). Likewise, the critical value of $T_{s,E119}$ (i.e., the average steel section temperature based on the thermocouple placement during an ASTM E119 standard fire test) at the onset of flexural runaway can be conservatively predicted using the load-dependent relationships of T_{cr} per Equation 4.22 from Eurocode 3, Part 1-2 (CEN, 2005) as well as AISC *Specification* Equation A-4-23.
- Based on the standard fire test data presented in this paper, these load-dependent critical temperature relationships for standard fire resistance are robust for SFRM-protected W8×28 floor beam assemblies that are restrained or unrestrained to thermal expansion, with composite or noncomposite reinforced concrete slabs (cast on corrugated metal decking). The quasi-standard test results in the published literature indicate that these critical temperature relationships may also be robust for section depths ranging from W8 to W18, the inclusion of shear tab connections (rather than unrealistic end-plate bearing connections, which are used in standard fire tests), the implementation of flat slabs (rather than those cast on corrugated metal decking), the material property details of the slab's concrete, unprotected steel beam sections (i.e., with no applied passive fire protection), variation in steel beam yield strength (with nominal ranging from 36–50 ksi), and span lengths ranging from 11 to 40 ft.
- The 3LM predictions of steel temperature for each flange and the web under standard fire exposure per Eurocode 4 slightly outperformed 1LM predictions of T_s for the entire section per Eurocode 3 and the AISC *Specification*. However, all LM predictions provided reasonably accurate and conservative estimations of standard fire resistance compared to those corresponding to flexural runaway of the AISC specimens tested to ASTM E119. The quality of these LM predictions depends on the temperature-dependent relationships that are used to calculate thermal properties of the steel and fire protection materials at each time step. Simplifying approximations were shown to be capable of conservatively predicting the steel temperature increase under standard fire exposure.

ACKNOWLEDGMENTS

Funding for this project was provided by the American Institute of Steel Construction (AISC) via the Milek Faculty Fellowship, of which Professor Quiel is the 2016 recipient. Additional funding to support Dr. Drury during his involvement in this research for his doctoral dissertation was provided by Lehigh University via a 2021 Faculty Innovation Grant. All experimental data and photos presented in this paper are reproduced with expressed written consent of AISC and AISI for the purposes of this study. Special thanks to Dr. Devin Huber (AISC) and Dr. Farid Alfawakhiri (AISI, retired) for their support of this project and for furnishing all data and documentation pertaining to the tests. All opinions, findings, and conclusions expressed in this paper are the authors' and do not necessarily represent the policies and views of AISC, AISI, or Lehigh University.

REFERENCES

AISC (2010), *Specification for Structural Steel Buildings,* ANSI/AISC 360-10, American Institute of Steel Construction, Chicago, Ill.

AISC (2022), *Specification for Structural Steel Buildings,* ANSI/AISC 360-22, American Institute of Steel Construction, Chicago, Ill.

Alfawakhiri, F., Carter, C.J., Berhing, R.M., Zeeveld, P., Hervey, F.E., and Woods, L.C. (2016), "The Effects of Load Intensity and Restraint on the Fire Resistance of Steel and Composite Beams," *9th International Conference on Structures in Fire SiF'16*, Princeton University, N.J.

ASCE (2007), *Standard Calculation Methods for Structural Fire Protection (ASCE/SEI/SFPE 29-05)*, American Society of Civil Engineers, Reston, Va.

ASCE (2020), *Performance-Based Structural Fire Design: Exemplar Designs of Four Regionally Diverse Buildings Using ASCE 7-16, Appendix E*, American Society of Civil Engineers, Reston, Va., doi: 10.1061/9780784482698.

ASTM (2019), *Test Methods for Fire Tests of Building Construction and Materials*, ASTM E119-19, ASTM International, West Conshohocken, Pa., doi: 10.1520/E0119–19.

ASTM (2020), *Standard Specification for Structural Steel Shapes*, ASTM A992–20, ASTM International, West Conshohocken, Pa., doi: 10.1520/A0992_A0992M-20.

ASTM (2022), *Standard Specification for Steel Wire and Welded Wire Reinforcement, Plain and Deformed, for Concrete*, ASTM A1064-22, ASTM International, West Conshohocken, Pa., doi: 10.1520/A1064_A1064M-22.

Berhinig, R.M. and Alfawakhiri, F. (2014), "New Fire Resistance Test for Loaded Unrestrained Beams," *ASCE/SEI Structures Congress*, American Society of Civil Engineers, Boston, Mass., pp. 1175–1184, doi: 10.1061/9780784413357.106.

Bletzacker, R.W. (1967), "Fire Resistance of Protected Steel Beam Floor and Roof Assemblies as Affected by Structural Restraint," *Symposium on Fire Test Methods—Restraint & Smoke 1966 (ASTM STP 422)*, ASTM International, West Conshohocken, Pa., pp. 63–90., doi: 10.1520/STP41306S.

Bono, J.A. (1970), "New Criteria for Fire Endurance Tests," *Fire Test Performance (ASTM STP 464)*, ASTM International, West Conshohocken, Pa., pp. 106–126, doi: 10.1520/STP44715S.

BSI (1987), *Fire Tests on Building Materials and Structures—Part 21: Methods for Determination of the Fire Resistance of Load-Bearing Elements of Construction*, BS 476-21:1987, British Standards Institute (BSI), London, UK.

BSI (2008), *Fire Tests on Building Materials and Structures. Part 10. Guide to the Principles, Selection, Role, and Application of Fire Testing and Their Outputs.*, BS 476-10:2009, British Standards Institute (BSI), London, UK.

Buchanan, A.H. and Abu, A. (2017), *Structural Design for Fire Safety*, 2nd Ed., John Wiley & Sons Inc., Chichester, West Sussex, UK.

CEN (2005), *EN 1993-1-2:2005 Eurocode 3: Design of Steel Structures—Part 1-2: General Rules—Structural Fire Design*, EN 1993–1-2:2005, European Committee for Standardization, Brussels, Belgium.

CEN (2008), *EN 1994–1-2:2005 Eurocode 4: Design of Composite Steel and Concrete Structures—Part 1-2: General Rules—Structural Fire Design*, European Committee for Standardization, Brussels, Belgium.

CEN (2009), *EN 1991–1-2:2002 Eurocode 1: Actions on Structures—Part 1-2: General Actions—Actions on Structures Exposed to Fire*, European Committee for Standardization, Brussels, Belgium.

Choe, L., Ramesh, S., Grosshandler, W., Hoehler, M., Seif, M., Gross, J., and Bundy, M. (2020), "Behavior and Limit States of Long-Span Composite Floor Beams with Simple Shear Connections Subject to Compartment Fires: Experimental Evaluation," *Journal of Structural Engineering*, Vol. 146, No. 6, p. 04020088, doi: 10.1061/(ASCE)ST.1943–541X.0002627.

Drury, M.M. (2022), *Critical Temperature Relationships for the Performance-Based Design of Realistically-Restrained Steel Composite Floor Assemblies*, Ph.D. Thesis, Lehigh University, Bethlehem, Pa.

Drury, M.M., Kordosky, A.N., and Quiel, S.E. (2020), "Structural Fire Resistance of Partially Restrained, Partially Composite Floor Beams, II: Modeling," *Journal of Constructional Steel Research*, Vol. 167, p. 105946, doi: 10.1016/j.jcsr.2020.105946.

Drury, M.M., Kordosky, A.N., and Quiel, S.E. (2021), "Robustness of a Partially Restrained, Partially Composite Steel Floor Beam to Natural Fire Exposure: Novel Validation and Parametric Analysis," *Journal of Building Engineering*, Vol. 44, p. 102533, doi: 10.1016/j.jobe.2021.102533.

Drury, M.M. and Quiel, S.E. (2023a), "Standard versus Natural Fire Resistance for Partially Restrained Composite Floor Beams: 1—Testing," *Journal of Constructional Steel Research*, Vol. 202, p. 107768, doi: 10.1016/j.jcsr.2022.107768.

Drury, M.M. and Quiel, S.E. (2023b), "Standard versus Natural Fire Resistance for Partially Restrained Composite Floor Beams: 2—Analysis," *Journal of Constructional Steel Research*, Vol. 202, p. 107767, doi: 10.1016/j.jcsr.2022.107767.

Franssen, J.-M. and Gernay, T. (2017), "Modeling Structures in Fire with SAFIR®: Theoretical Background and Capabilities," *Journal of Structural Fire Engineering*, Vol. 8, No. 3, pp. 300–323, doi: 10.1108/JSFE-07–2016–0010.

Gamble, W.L. (1989), "Predicting Protected Steel Member Fire Endurance Using Spread-Sheet Programs," *Fire Technology*, Vol. 25, No. 3, pp. 256–273, doi: 10.1007/BF01039782.

Ghojel, J.I. and Wong, M.B. (2005), "Three-Sided Heating of I-Beams in Composite Construction Exposed to Fire," *Journal of Constructional Steel Research*, Vol. 61, No. 6, pp. 834–844, doi: 10.1016/j.jcsr.2004.11.006.

ICC (2020), *IBC: International Building Code, 2021*, International Code Council, Country Club Hills, Ill.

ISO (2019), *Fire Resistance Tests—Elements of Building Construction—Part 11: Specific Requirements for the Assessment of Fire Protection to Structural Steel Elements*, ISO 834–11:2014, International Organization for Standardization, Geneva, Switzerland.

Jiang, S.-C., Ranzi, G., Chen, L.-Z., and Li, G.-Q. (2017), "Behaviour and Design of Composite Beams with Composite Slabs at Elevated Temperatures," *Advances in Structural Engineering*, Vol. 20, No. 10, pp. 1451–1465, doi: 10.1177/1369433216682507.

Khorasani, N.E., Gardoni, P., and Garlock, M. (2015), "Probabilistic Fire Analysis: Material Models and Evaluation of Steel Structural Members," *Journal of Structural Engineering*, Vol. 141, No. 12, p. 04015050, doi: 10.1061/(ASCE)ST.1943–541X.0001285.

Kordosky, A.N., Drury, M.M., and Quiel, S.E. (2020), "Structural Fire Resistance of Partially Restrained, Partially Composite Floor Beams, I: Experiments," *Journal of Constructional Steel Research*, Vol. 167, p. 105945, doi: 10.1016/j.jcsr.2020.105945.

LaMalva, K., Bisby, L., Gales, J., Gernay, T., Hantouche, E., Jones, C., Morovat, A., Solomon, R., and Torero, J. (2020), "Rectification of 'Restrained vs Unrestrained'," *Fire and Materials*, Vol. 44, No. 3, pp. 341–351, doi: 10.1002/fam.2771.

LaMalva, K.J. (Ed.). (2018), *Manual of Practice 138: Structural Fire Engineering*, American Society of Civil Engineers, Reston, Va.

Newman, G. (1999), "The Cardington Fire Tests," *Proceedings of the North American Steel Construction Conference*, AISC, Toronto, Canada, pp. 28.1–28.22.

Ruddy, J., Marlo, J., Ioannides, S., and Alfawakhiri, F. (2003), *Fire Resistance of Structural Steel Framing*, Design Guide 19, AISC, Chicago, Ill.

Selden, K.L. and Varma, A.H. (2016), "Composite Beams under Fire Loading: Numerical Modeling of Behavior," *Journal of Structural Fire Engineering*, Vol. 7, No. 2, pp. 142–157, doi: 10.1108/JSFE-06–2016–011.

UL (2019a), *Fire Resistance Directory*, Underwriters Laboratories Inc., Northbrook, Ill.

UL (2019b), *Fire Resistance Directory: Design No. D982*, Underwriters Laboratories Inc., Northbrook, Ill.

UL (2020), *Standard for Fire Tests of Building Construction and Materials*, UL 263, Underwriters Laboratories, Inc., Northbrook, Ill.

Vinnakota, M.R., Foley, C.M., and Vinnakota, S. (1988), "Design of Partially or Fully Composite Beams with Ribbed Metal Deck Using LRFD Specifications," *Engineering Journal,* AISC, Vol. 25, No. 2, pp. 60–78.

Wang, W., Engelhardt, M.D., Li, G., and Huang, G. (2017), "Behavior of Steel–Concrete Partially Composite Beams Subjected to Fire—Part 1: Experimental Study," *Fire Technology*, Vol. 53, No. 3, pp. 1039–1058, doi: 10.1007/s10694–016–0618-y.

Zhao, B. and Kruppa, J. (1997), *Fire Resistance of Composite Slabs with Profiled Steel Sheet and of Composite Steel Concrete Beams, Part 2: Composite Beams Final Report*, Office for Official Publications of the European Communities, Luxembourg.

Generalized Elastic Lateral-Torsional Buckling of Steel Beams

ROBERT S. GLAUZ and BENJAMIN W. SCHAFER

ABSTRACT

A concise review is provided of the classical elastic lateral-torsional buckling moment for steel beams as utilized in the AISC *Specification* (2022). Rather than make assumptions regarding the cross-section properties, the derivation is provided in its general form for an arbitrary steel beam—that is, one that may be asymmetric and may include any manner of varying geometry, thickness, or cross-section shape. The cross-section properties that underpin the calculation are fully detailed. The assumptions that are inherent in the classical derivations (no shear, no cross-section distortion, etc.) are also fully detailed. The manner in which the generalized lateral-torsional buckling formula may be simplified for particular sections (e.g., a singly symmetric channel) with no loss of accuracy is explained. Adaptations and approximations utilized in the 2022 edition of the AISC *Specification* for elastic lateral-torsional buckling moment of specific sections (e.g., mono-symmetric I-section, angles, etc.) are assessed against the actual elastic solution, and the accuracy and clarity of the assumptions utilized are evaluated. The generalized formula, consistent with current assumptions but applicable to all structural steel cross sections, is recommended for future reference in the main body of the AISC *Specification*.

Keywords: lateral-torsional buckling, elastic buckling, steel beams.

INTRODUCTION

Steel beams with large unbraced spans are susceptible to lateral-torsional buckling. This instability is manifested by simultaneous lateral translation and twisting of the member, as shown in Figure 1. Upon lateral-torsional buckling, the beam is unable to carry additional load due to the formation of plastic mechanisms in the cross section triggered by the buckling that ultimately result in localized loss of stiffness and the potential for collapse. Slender members with narrow cross sections and long unbraced lengths are more susceptible to lateral-torsional buckling.

An early example of lateral-torsional buckling failure, before this mechanism was better understood, was the collapse of the Dee Bridge in Chester, England. Built in 1846 for rail transportation, the main girders were 45 in. deep cast iron with 24-in.-wide bottom flanges but only 7-in.-wide top compression flanges. Lateral-torsional instability (among other factors) led to the collapse during the crossing of a multi-car passenger train in 1847 (Commissioners of Railways, 1848). Bridge engineers learned from this and other failures that the compression flange must be stabilized or increased in size to prevent buckling.

The AISC *Specification for Structural Steel Buildings*, hereafter referred to as the AISC *Specification*, has evolved significantly over its history. The first edition (AISC, 1923) protected against lateral-torsional buckling in a simple, but effective and safe manner, treating the compression flange as a column expressing strength as a function of slenderness (L/b), where L is the beam length and b is the compression flange width. Column stability was reasonably well understood based on the early work of Euler (1744), although the mathematics of beam elastic lateral-torsional buckling was not formalized until later by Timoshenko (1936). As shown in Figure 2, the design bending stress F_b was reduced as L/b increased from 15 to an upper limit of 40. This upper limit ensured sufficient stability to prevent elastic buckling failure. The 1936 edition of the AISC *Specification* continued using the same approach, allowing higher stress consistent with the higher yield strength of A9 structural steel at that time.

By the 1946 edition (AISC, 1946), the mechanics of elastic lateral-torsional buckling were better understood. The two components of torsional stiffness for a doubly symmetric I-section can be approximated in terms of $(L/b)^2$ for the warping resistance and Ld/bt for the pure torsion resistance (Salmon and Johnson, 1980). For the vast majority of I-sections used in construction at the time, the flanges were thick enough for the pure torsion resistance to dominate. Therefore, the lateral-torsional buckling design stress changed to a form using slenderness Ld/bt, where d is the depth of the section and t is the thickness of the flange. As shown in Figure 2, this significantly increased the design stress for many I-sections and the upper limit on slenderness was removed.

Robert S. Glauz, Owner, RSG Software, Inc., Lee's Summit, Mo. Email: glauz@rsgsoftware.com (corresponding)

Benjamin W. Schafer, Professor, Johns Hopkins University, Baltimore, Md. Email: schafer@jhu.edu

Paper No. 2024–08

The 1961 edition (AISC, 1961) continued with the same design stress expression using Ld/bt. Due to the introduction of A36 steel and the availability of different steel grades, this was the first edition to incorporate the material yield strength F_y into the provisions. This edition also recognized that deeper I-sections with thinner flanges could achieve higher strength due to the warping resistance. Therefore, the design stress was permitted to be the larger of the 1946 formula and a new inelastic buckling expression utilizing $(L/r)^2$. Instead of the compression flange width b, this formula used r, defined as the radius of gyration of a tee section comprising the compression flange plus ⅙ of the web area, which is approximately $0.27b$ for a rectangular flange. This generalization accommodated the use of flange geometries other than rectangular. The 1961 edition also included a Commentary that acknowledged the existence of more accurate calculation methods stating: "Rational expressions for the elastic buckling strength of the beam, which take into account its torsional rigidity about its longitudinal axis as well as the bending stiffness of its compression flange, are too complex for general office use." Tables of torsional properties did not appear in the AISC *Steel Construction Manual*, hereafter referred to as the AISC *Manual*, until the eighth edition (AISC, 1981).

It wasn't until the 1986 LRFD edition (AISC, 1986) that both components of torsional stiffness were combined to correctly calculate the critical buckling moment for an I-section, rather than the larger of the two components. As a theoretically accurate calculation, its use was later extended to singly symmetric channel sections and may actually be used for any section bending about an axis of symmetry. This edition also provided approximations to the theoretical solution for other sections that are not symmetrical about the axis of bending. These and other approximations unique to particular cross sections are still in use in the current edition of the AISC *Specification* (2022).

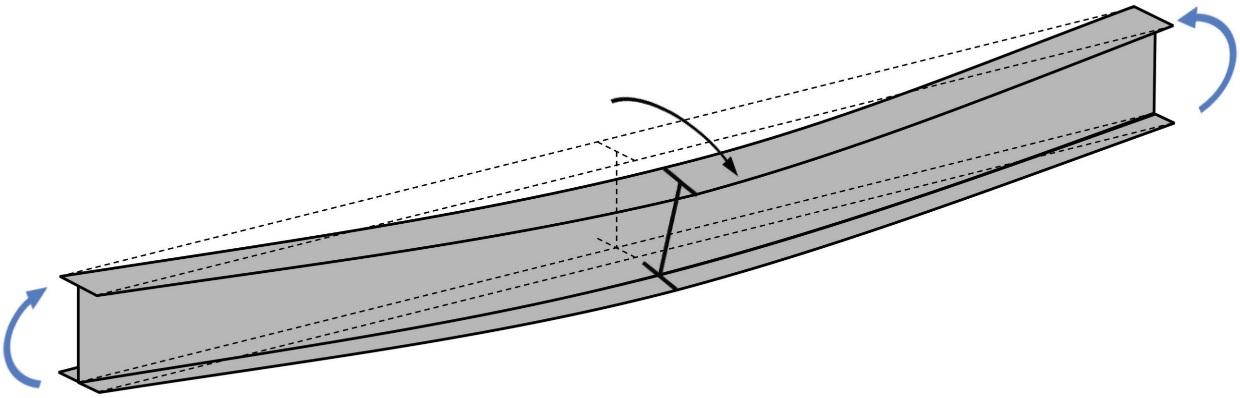

Fig. 1. Lateral-torsional buckling—translation and twist.

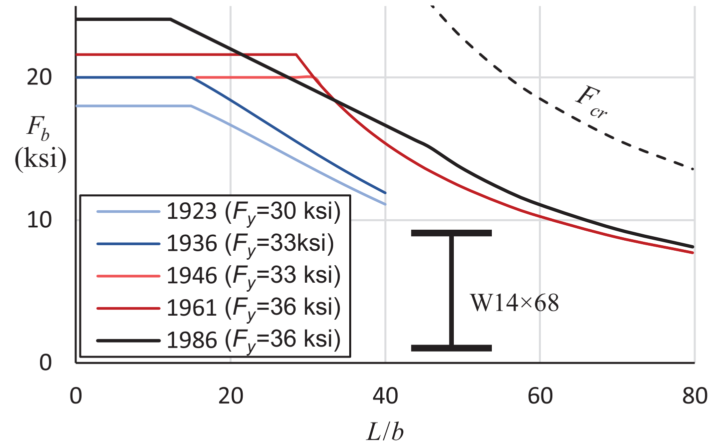

Fig. 2. AISC history of design stress for lateral-torsional buckling.

Figure 2 also illustrates that the 1986 strength permitted moments up to full plasticity, where the allowable design stress is shown as $M_p/1.67S_x$. A new inelastic buckling strength was implemented using a linear transition between the fully plastic moment and the elastic buckling moment.

This paper focuses on determination of the elastic lateral-torsional buckling moment and does not attempt to address inelastic buckling strength. The purpose is to show that the elastic buckling moment calculation can be applied in a consistent way for all cross sections without the approximations that can result in unacceptable error, thus providing a unified approach for all cross sections.

ELASTIC THEORY

The classic approach to the elastic buckling solution of a linear prismatic member is to consider only end forces. The application of axial load P at eccentricities $e_{\dot{x}}$ and $e_{\dot{y}}$ as shown in Figure 3 provides a general solution for a beam-column undergoing any combination of axial load and uniform moments.

Assuming small displacements such that the longitudinal stresses remain constant throughout the member length (first-order analysis), the three equations of equilibrium as expressed by Timoshenko and Gere (1961) are given as:

$$EI_{\dot{y}}\dot{u}^{iv} + P\dot{u}'' + P(\dot{y}_o - e_{\dot{y}})\phi'' = 0 \tag{1}$$

$$EI_{\dot{x}}\dot{v}^{iv} + P\dot{v}'' + P(\dot{x}_o - e_{\dot{x}})\phi'' = 0 \tag{2}$$

$$\begin{aligned} EC_w\phi^{iv} - (GJ - \beta_{\dot{x}}Pe_{\dot{y}} - \beta_{\dot{y}}Pe_{\dot{x}} - Pr_o^2)\phi'' \\ + P(\dot{y}_o - e_{\dot{y}})\dot{u}'' - P(\dot{x}_o - e_{\dot{x}})\dot{v}'' = 0 \end{aligned} \tag{3}$$

where $\dot{x}$ and $\dot{y}$ are the principal axes of the cross section, $\dot{u}$ and $\dot{v}$ are translational displacements in the $\dot{x}$ and $\dot{y}$ directions, ϕ is twisting displacement, E is the modulus of elasticity, G is the shear modulus, and the other variables are geometric properties of the cross section ($I_{\dot{x}}$, $I_{\dot{y}}$, C_w, J, $\dot{x}_o$, $\dot{y}_o$, r_o, $\beta_{\dot{x}}$, $\beta_{\dot{y}}$). To solve these differential equations for warping-free pinned end conditions, the displacements ($\dot{u}$, $\dot{v}$, ϕ) are assigned sinusoidal forms of one half-wavelength, end translation and twist are restrained ($\dot{u} = \dot{v} = \phi = 0$), and end moments and bimoments are zero ($\dot{u}'' = \dot{v}'' = \phi'' = 0$). The result is three simultaneous equations solved by equating the determinant of the coefficients to zero:

$$\begin{bmatrix} P_{e\dot{y}} - P & 0 & -P\dot{y}_o + M_{\dot{x}} \\ 0 & P_{e\dot{x}} - P & P\dot{x}_o - M_{\dot{y}} \\ -P\dot{y}_o + M_{\dot{x}} & P\dot{x}_o - M_{\dot{y}} & (P_t - P)r_o^2 - \beta_{\dot{x}}M_{\dot{x}} - \beta_{\dot{y}}M_{\dot{y}} \end{bmatrix} \tag{4}$$

$$\begin{Bmatrix} \dot{u} \\ \dot{v} \\ \phi \end{Bmatrix} = \begin{Bmatrix} 0 \\ 0 \\ 0 \end{Bmatrix}$$

where $M_{\dot{x}}$ ($Pe_{\dot{y}}$) and $M_{\dot{y}}$ ($Pe_{\dot{x}}$) are the end moments produced by the axial eccentricities, and $P_{e\dot{x}}$, $P_{e\dot{y}}$, and P_t are the axial loads at which elastic buckling occurs about the $\dot{x}$-axis, about the $\dot{y}$-axis, and in torsion, respectively:

$$P_{e\dot{x}} = \frac{\pi^2 EI_{\dot{x}}}{L^2} \tag{5}$$

$$P_{e\dot{y}} = \frac{\pi^2 EI_{\dot{y}}}{L^2} \tag{6}$$

$$P_t = \frac{1}{r_o^2}\left(GJ + \frac{\pi^2 EC_w}{L^2}\right) \tag{7}$$

The case of interest for lateral-torsional buckling is bending about the major principal axis. Using $\dot{x}$ as the major principal axis, the eccentricity $e_{\dot{y}}$ is increased as the axial load P approaches zero. In the limit, $P = 0$, $M_{\dot{y}} = 0$, and $M_{\dot{x}}$ is the critical moment for buckling about the $\dot{x}$ axis given by the equation:

$$M_{\dot{x}}^2 + \beta_{\dot{x}}P_{e\dot{y}}M_{\dot{x}} - r_o^2 P_{e\dot{y}}P_t = 0 \tag{8}$$

The general solution to this quadratic has two roots representing the critical moments for positive and negative bending (±$e_{\dot{y}}$). For beams bending about a non-principal x-axis, the elastic lateral-torsional buckling moment is given by the same formula as shown in Glauz (2017), with

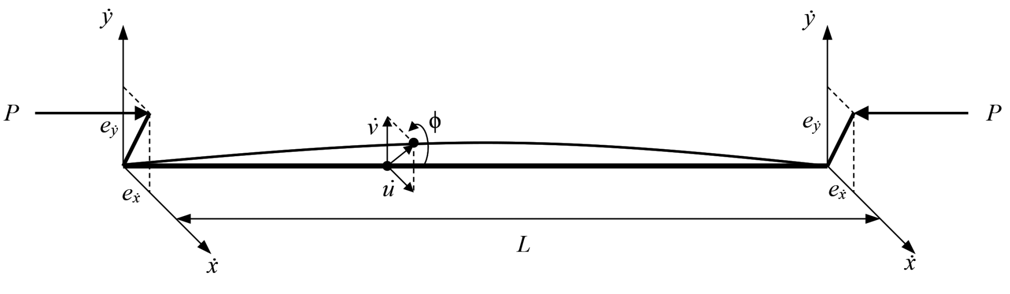

Fig. 3. Beam-column elastic buckling problem.

a more generalized expression for the flexural buckling component.

$$M_x^2 + \beta_x P_{ey} M_x - r_o^2 P_{ey} P_t = 0 \tag{9}$$

$$P_{ey} = \frac{\pi^2 E I_y}{L^2}\left(1 - \frac{I_{xy}^2}{I_x I_y}\right) = \frac{\pi^2 E}{L^2}\left(\frac{I_x I_y - I_{xy}^2}{I_x}\right) = \frac{\pi^2 E I_{\dot{x}} I_{\dot{y}}}{L^2 I_x} \tag{10}$$

where I_x and I_y are the moments of inertia about any orthogonal x- and y-axes (often the geometric axes of the section), and I_{xy} is the product of inertia. As the x-axis approaches the principal $\dot{x}$-axis, the product of inertia I_{xy} approaches zero and P_{ey} becomes $P_{e\dot{y}}$.

OTHER CONSIDERATIONS

The preceding development assumes small displacements and the results agree with numerical elastic buckling analyses based on first-order internal stresses. In reality, displacements prior to buckling (second-order effects) alter the buckling response. For bending about the x-axis, deflection in the y-direction prior to buckling provides a stabilizing effect and enables a higher buckling moment. The closer the ratio I_y/I_x approaches 1, the greater the increase in buckling moment. For $I_y > I_x$, the x-axis is no longer the major axis, and lateral-torsional buckling is unlikely to occur, although still possible for unsymmetrical sections with large β_x magnitude, low torsional stiffness, and shear center in tension.

In addition, the preceding solution assumes no distortion occurs within the cross section as the member undergoes lateral-torsional buckling. If the web is slender enough, destabilization of the flange during lateral-torsional buckling may result in section distortion—often referred to as elastic lateral-distortional buckling (Bradford, 1992). This mode of buckling may be especially likely when bracing is only present for the compression flange and not the full member depth. Further, elastic local plate buckling in the section (another form of potential distortion in the section) and its potential interaction with lateral-torsional buckling are not covered here.

The provided buckling solution assumes warping-free pinned end conditions—that is, translation and twisting are restrained, and rotation and warping are free at both ends. Other end conditions where flexural and twisting wavelengths align will yield the same solution, except with L replaced by the half-wavelength KL, where K is an effective length factor. As an example, fixing the rotation and warping at both ends corresponds to $K = 0.5$. For boundary conditions where flexural and twisting wavelengths do not align, the solution is more complex. However, the critical moment can be approximated using different KL values for the flexural component, P_{ey}, and the torsional component, P_t.

The buckling solution (Equation 8) is also based on a uniform moment induced by equal and opposite end moments. The elastic buckling moment for unequal end moments has historically been handled in the AISC *Specification* by approximation using a multiplicative bending coefficient C_b, based on the ratio of the end moments as given by Equation 11, where M_2 is the larger end moment and the ratio $M_1/M_2 = -1$ for uniform moment.

$$C_b = 1.75 + 1.05\frac{M_1}{M_2} + 0.30\left(\frac{M_1}{M_2}\right)^2 \le 2.3 \tag{11}$$

This C_b coefficient increases the buckling moment by up to 2.3 times the uniform moment case, where the resulting buckling moment is the magnitude at the M_2 end. Further, Equation 11 for C_b assumes a linear moment diagram; however, the primary application for beams involves transverse loading and thus a nonlinear moment diagram (e.g., parabolic for uniform load). Many codes use the refined bending coefficient shown in Equation 12 to more accurately approximate the buckling moment for unbraced spans with transverse loads. It is a slight variation of the expression developed by Kirby and Nethercot (1979), which uses the absolute value of applied moments at the quarter points (M_A, M_B, M_C) and the maximum moment (M_{max}) within the unbraced span. This multiplier ranges from 1.0 to 5.0, and the resulting buckling moment is the magnitude at the location of M_{max}.

$$C_b = \frac{12.5 M_{max}}{2.5 M_{max} + 3M_A + 4M_B + 3M_C} \tag{12}$$

Other bending coefficient expressions have been developed to approximate the buckling moment for some specific cases, such as Wong and Driver (2010) for doubly symmetric I-shape beams, Helwig et al. (1997) for singly symmetric I-shape beams, and Yura (1995) for interior span of I-shape beams with top flange lateral restraint.

The application of transverse loads also produces shear stresses in the member. The elastic buckling solution leading to Equation 8 does not consider shear stresses, which for slender beams are minor compared to longitudinal stresses; however, Liang et al. (2022) have shown cases where shear stresses are important to consider and provided modifications to the classic formula. The location of transverse load application can also influence the lateral-torsional buckling behavior. For a vertical load applied with a horizontal offset from the shear center, torsional forces are applied to the member. The resulting pre-buckling torsional displacements can adversely affect the torsional and flexural components of the lateral-torsional buckling response. For a vertical load applied with a vertical offset from the shear center the load application point can either increase or decrease the buckling moment. For a downward load applied to a beam above the shear center, small rotation of the member prior to buckling will be amplified by the additional torque induced by the load location and decrease the buckling moment. On the other hand, a downward load applied below the shear center will counteract any small rotation of the member prior to buckling and increase the buckling moment. Some design codes such as Eurocode 3 (CEN, 2005) provide additional coefficients to account for the load height effect, and the AISC *Specification* provides additional references in its Commentary.

All of these considerations are excluded from the formulas presented in this article, except that the commonly used bending moment gradient coefficient C_b is included for consistency and clarity.

SECTION PROPERTIES

The elastic buckling solution is applicable to a member of any cross section. The section properties required to determine the buckling moment about the x-axis are the moments of inertia, I_x and I_y, the product of inertia, I_{xy}, the torsional warping constant, C_w, the St. Venant torsional constant, J, the polar radius of gyration about the shear center, r_o, and a unique asymmetry property, β_x. Figure 4 shows a general unsymmetrical cross section with x- and y-axes passing through the centroid, c, along with the location of the shear center, o, and asymmetry point, a. The centroid is the location where axial loads produce no moments, the shear center is the location where transverse loads produce no torsion, and the asymmetry point is the offset from the shear center that produces torsional geometric stiffness due to flexure. The vector from the shear center to the asymmetry point is half of β, and the component of that vector perpendicular to the x-axis is $\beta_x/2$.

Analysis of the longitudinal stresses resulting from compression and flexure require integration over the area of the cross section. These integrations correspond to the familiar terms area, A, moments of inertia about the x- and y-axes, I_x and I_y, the product of inertia, I_{xy}, the polar moment of inertia about the centroid, I_c, and the radius of gyration about the centroid, r_c. The angle to the principal axes, α, and the principal axis moments of inertia, $I_{\dot{x}}$ and $I_{\dot{y}}$, are also given.

$$A = \int_A dA \tag{13}$$

$$I_x = \int_A y^2\, dA \tag{14}$$

$$I_y = \int_A x^2\, dA \tag{15}$$

$$I_{xy} = \int_A xy\ dA \tag{16}$$

$$I_c = \int_A (x^2 + y^2)\, dA = I_x + I_y \tag{17}$$

$$r_c = \sqrt{I_c/A} = \sqrt{I_x/A + I_y/A} = \sqrt{r_x^2 + r_y^2} \tag{18}$$

$$\alpha = \frac{1}{2}\arctan\frac{-2I_{xy}}{I_x - I_y} \tag{19}$$

$$I_{\dot{x}}, I_{\dot{y}} = \frac{1}{2}(I_x + I_y) \pm \frac{1}{2}\sqrt{(I_x - I_y)^2 + 4I_{xy}^2} \tag{20}$$

Analysis of the stresses resulting from torsion first require determination of the torsion axis, or shear center of the cross section. The shear center is the point (x_o, y_o) in the cross section where an applied shear force in any transverse direction produces no torsion. The polar moment of inertia, I_o, and radius of gyration, r_o, about the shear center are similar to those about the centroid, but greater due to the offset of the shear center. The warping constant, C_w, is a measure of torsional stiffness due to warping, analogous to the moment of inertia, I, and bending stiffness due to flexure. The St. Venant torsional constant, J, is a measure of torsional stiffness due to pure torsion.

The distribution of torsional stresses can be difficult to determine for a general cross section. Numerical methods

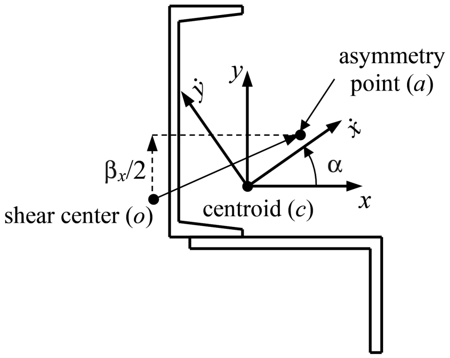

Coordinate Transformations

$$\dot{x} = x\cos\alpha + y\sin\alpha$$
$$\dot{y} = y\cos\alpha - x\sin\alpha$$

$$x = \dot{x}\cos\alpha - \dot{y}\sin\alpha$$
$$y = \dot{y}\cos\alpha + \dot{x}\sin\alpha$$

Fig. 4. Properties of general unsymmetrical cross section.

utilizing finite elements of the cross section are useful for irregular shapes. Computer software is available for this task such as MSASect2 (2023), ShapeBuilder (2023), and Sectionproperties open-source code (2024). For thin-walled open sections, these properties are more readily calculable using sectorial coordinates (ω_c, ω_o, ω_n) and integrating over distance s along the midlines of the cross-section elements of thickness t. These integrations are given as follows:

$$x_o = \frac{I_y \int_0^l \omega_c y t \, ds - I_{xy} \int_0^l \omega_c x t \, ds}{I_x I_y - I_{xy}^2} \tag{21}$$

$$y_o = \frac{I_x \int_0^l \omega_c x t \, ds - I_{xy} \int_0^l \omega_c y t \, ds}{I_x I_y - I_{xy}^2} \tag{22}$$

$$I_o = \int_A \left[(x - x_o)^2 + (y - y_o)^2 \right] dA = I_c + A x_o^2 + A y_o^2 \tag{23}$$

$$r_o = \sqrt{I_o / A} = \sqrt{r_c^2 + x_o^2 + y_o^2} \tag{24}$$

$$C_w = \int_0^l \omega_n^2 t \, ds = \int_0^l \omega_o^2 t \, ds - A \bar{\omega}_o^2 \tag{25}$$

$$\omega_c = \int_0^s \rho_c \, ds \tag{26}$$

$$\omega_o = \int_0^s \rho_o \, ds \tag{27}$$

$$\omega_n = \omega_o - \bar{\omega}_o = \omega_o - \frac{1}{A} \int_0^l \omega_o t \, ds \tag{28}$$

$$J = \frac{1}{3} \int_0^l t^3 \, ds \tag{29}$$

The variables ρ_c and ρ_o are the perpendicular distances to the element midline, measured from the centroid and shear center, respectively. The details of the sectorial coordinate calculations are given in several texts such as Timoshenko and Gere (1961), Yu (2000), and Liu et al. (2018).

Torsional equilibrium given by Equation 3 shows that the coefficient on ϕ'' is the pure torsion elastic stiffness GJ counteracted by the torsion geometric stiffness ($M_{\dot{x}} \beta_{\dot{x}} + M_{\dot{y}} \beta_{\dot{y}} + P r_o^2$), which is produced by the distribution of normal stresses over the cross section resulting from the applied forces $M_{\dot{x}}$, $M_{\dot{y}}$, and P. Based on the work by Glauz (2017), it can be shown that $M_{\dot{x}} \beta_{\dot{x}} + M_{\dot{y}} \beta_{\dot{y}} = M_x \beta_x + M_y \beta_y$; therefore, the β properties associated with the geometric x- and y-axes may be used with the moments about these axes. The properties β_x and β_y are distances given by Equations 30 and 31, equal to twice the orthogonal distances from the shear center (x_o, y_o) to the asymmetry point (x_a, y_a). The coordinates of the asymmetry point are calculated using integrations over the cross-sectional area without the need for thin-walled assumptions.

$$\beta_x = 2(y_a - y_o) \tag{30}$$

$$\beta_y = 2(x_a - x_o) \tag{31}$$

$$y_a = \frac{U_x I_y - U_y I_{xy}}{2(I_x I_y - I_{xy}^2)} \tag{32}$$

$$x_a = \frac{U_y I_x - U_x I_{xy}}{2(I_x I_y - I_{xy}^2)} \tag{33}$$

$$U_x = \int_A y^3 \, dA + \int_A x^2 y \, dA \tag{34}$$

$$U_y = \int_A x^3 \, dA + \int_A y^2 x \, dA \tag{35}$$

For bending about a geometric axis, the properties required to calculate M_{cr} may be calculated using the preceding formulas without transforming coordinates to the principal axes. If the geometric axes are the principal axes, $I_{xy} = 0$ and the formulas for x_o, y_o, x_a, and y_a are simplified. For bending about a principal axis that is not the geometric axis, the necessary section properties may either be calculated as given above and the coordinates x_o, y_o, x_a, and y_a transformed to the rotated principal axes, or all the properties could be calculated using rotated principal axis $\dot{x}$ and $\dot{y}$ coordinates. Note, for a doubly symmetric section, the asymmetry point and the shear center coincide with the centroid, thus all the properties x_o, y_o, x_a, y_a, β_x, and β_y are equal to 0, and the formulas greatly simplify.

APPLICATION

The solution to the quadratic given by Equation 8 is shown below, where M_{cr} is the elastic critical moment about the $\dot{x}$ (major principal)-axis.

$$M_{cr} = C_b P_{e\dot{y}} \left[-\frac{\beta_{\dot{x}}}{2} \pm \sqrt{\left(\frac{\beta_{\dot{x}}}{2} \right)^2 + \frac{r_o^2 P_t}{P_{e\dot{y}}}} \right] \tag{36}$$

An expanded form for M_{cr} is also shown in Equation 37, where P_t and $P_{e\dot{y}}$ have been replaced by their respective expressions.

$$M_{cr} = C_b \frac{\pi^2 E I_{\dot{y}}}{L^2} \left[-\frac{\beta_{\dot{x}}}{2} \pm \sqrt{\left(\frac{\beta_{\dot{x}}}{2} \right)^2 + \frac{G J L^2}{\pi^2 E I_{\dot{y}}} + \frac{C_w}{I_{\dot{y}}}} \right] \tag{37}$$

Equation 36 has the advantage of compactness and commonality with variables used for column buckling; Equation 37 explicitly reveals the influence of unbraced length L and eliminates the r_o property.

Two M_{cr} solutions are given by the positive and negative roots, where the positive root corresponds to a positive moment about the $\dot{x}$ axis—that is, compression on the positive $\dot{y}$ side of the $\dot{x}$-axis ($e_{\dot{y}} > 0$, top flange in compression). Design codes typically provide the magnitude of the buckling moment as a positive number; therefore, the negative root should be negated by multiplying through by −1. This makes the radical additive and changes the sign on the $\beta_{\dot{x}}/2$

term to positive for negative bending. The following form handles this with the C_s sign coefficient having a value of +1 for negative moment ($e_{\dot{y}} < 0$, bottom flange in compression) and −1 for positive moment ($e_{\dot{y}} > 0$, top flange in compression); resulting in:

$$M_{cr} = C_b P_{e\dot{y}} \left[C_s \frac{\beta_{\dot{x}}}{2} + \sqrt{\left(\frac{\beta_{\dot{x}}}{2}\right)^2 + \frac{r_o^2 P_t}{P_{e\dot{y}}}} \right] \tag{38}$$

or

$$M_{cr} = C_b \frac{\pi^2 E I_{\dot{y}}}{L^2} \left[C_s \frac{\beta_{\dot{x}}}{2} + \sqrt{\left(\frac{\beta_{\dot{x}}}{2}\right)^2 + \frac{GJL^2}{\pi^2 E I_{\dot{y}}} + \frac{C_w}{I_{\dot{y}}}} \right] \tag{39}$$

For bending about a non-principal x-axis, the elastic lateral-torsional buckling moment is determined from Equation 9 with P_t and P_{ey} replaced by their expressions from Equations 7 and 10, respectively:

$$M_{cr} = C_b \frac{\pi^2 E (I_x I_y - I_{xy}^2)}{L^2 I_x} \left[C_s \frac{\beta_x}{2} + \sqrt{\left(\frac{\beta_x}{2}\right)^2 + \frac{(GJL^2 + \pi^2 E C_w) I_x}{\pi^2 E (I_x I_y - I_{xy}^2)}} \right] \tag{40}$$

As will be discussed, Equation 40 applies to every cross section utilized in the AISC *Specification*. There is only one formula necessary for predicting the elastic lateral-torsional buckling moment of all steel sections under the assumptions previously stated.

It can be useful to determine the unbraced length L corresponding to any critical moment M_{cr}. Solving Equation 39 (principal axis bending) for L^2 gives the following expression:

$$L^2 = \frac{C_b \pi^2 E I_{\dot{y}}}{M_{cr}} \left[C_s \frac{\beta_{\dot{y}}}{2} + \frac{C_b GJ}{2M_{cr}} + \sqrt{\left(C_s \frac{\beta_{\dot{x}}}{2} + \frac{C_b GJ}{2M_{cr}} \right)^2 + \frac{C_w}{I_{\dot{y}}}} \right] \tag{41}$$

The AISC *Specification* presumes that transitions in strength may occur when M_{cr} reaches a given moment—for example, M_r. Therefore, the length L_r where $M_{cr} = M_r$ may be found by simple substitution into Equation 41:

$$L_r^2 = \frac{C_b \pi^2 E I_{\dot{y}}}{M_r} \left[C_s \frac{\beta_{\dot{y}}}{2} + \frac{C_b GJ}{2M_r} + \sqrt{\left(C_s \frac{\beta_{\dot{x}}}{2} + \frac{C_b GJ}{2M_r} \right)^2 + \frac{C_w}{I_{\dot{y}}}} \right] \tag{42}$$

Calculating M_{cr} requires the section properties $I_{\dot{y}}$, J, C_w, and $\beta_{\dot{x}}$. The $I_{\dot{y}}$ property is readily available for standard shapes and easily calculated for others, whereas the other properties are used less frequently and can be more difficult to calculate. The following subsections discuss these properties for different cases. Formulas are provided for many of these properties using midline dimensions and thin-walled assumptions, ignoring fillets. Full integration including fillets is available in software tools such as those previously mentioned and could be predetermined and tabulated for standard shapes as is done currently for J and C_w in the AISC *Manual* (2023).

Bending about Axis of Symmetry

Figure 5 illustrates several common shapes bending about the axis of symmetry, which is both the geometric x-axis and the principal $\dot{x}$-axis ($I_{xy} = 0$). This symmetry results in $\beta_x = 0$ because the shear center and asymmetry point lie on the axis of symmetry ($y_o = y_a = 0$). The elastic buckling

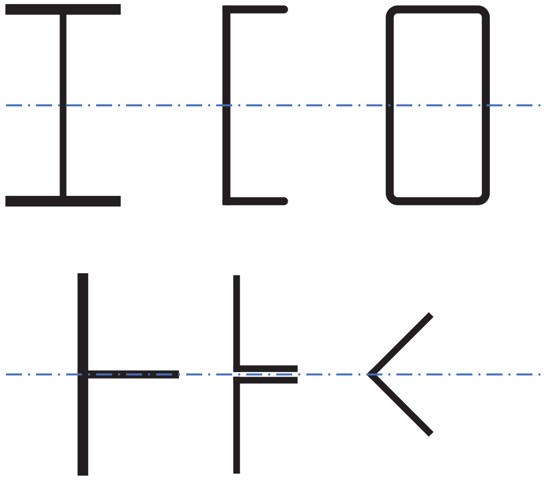

Fig. 5. Sections bending about the axis of symmetry.

equation then simplifies to the following, which is also given in a User Note of the AISC *Specification* (2022) Section F2:

$$M_{cr} = C_b r_o \sqrt{P_{ey} P_t} = C_b \frac{\pi}{L} \sqrt{EI_y \left(GJ + \frac{\pi^2}{L^2} EC_w \right)} \quad (43)$$

For doubly symmetric I-sections (W, M, S, HP) and channels (C, MC), the torsional properties J and C_w are given in AISC *Manual* (2023) tables. For rectangular HSS, tee (WT, MT, ST), double-angle sections, and equal-leg angles, J is given in the AISC *Manual* tables, whereas C_w is much less significant and ignored in the AISC *Specification*. Thick flanges and large fillets increase C_w, which can be computed using numerical methods.

Box Sections

Figure 6 shows a hollow rectangular box section with dimensional parameters and formulas for the required section properties. This section is doubly symmetric, thus $\beta_x = 0$, and Equation 43 is applicable.

Mono-Symmetric I-Section

Figure 7 shows a general mono-symmetric I-section with dimensional parameters and formulas for the required section properties. The C_s sign coefficient corresponds to the direction of the applied moment, but the sign of $\beta_x/2$ is also important and must be calculated properly. The $\beta_x/2$ value is negative when the larger flange is on the positive y-side of the x-axis for I-sections with typical proportions ($t_1 = t_2 > t_w$, $b_2 < b_1 < d_c$).

Tee Section

Figure 8 shows a general tee section with dimensional parameters and formulas for the required section properties. The $\beta_x/2$ value is negative when the flange is on the positive y-side of x-axis for tee sections with typical proportions ($t_1 > t_w$, $b_1 < 2d_c$). The shear center is at the intersection of the flange and web, therefore C_w can be taken as 0.

Double Angle

Back-to-back angle sections are similar to tee sections but with an optional spacing between the vertical legs. Figure 9 shows general back-to-back angles with dimensional parameters and formulas for the required section properties. The $\beta_x/2$ value is negative when the flanges are on the positive y-side of x-axis for typical double angle proportions ($2s_c < b_c < d_c$). The shear center is at the intersection of the flanges and axis between the vertical legs. For close spacings, C_w is small and can be taken as 0.

Single Angle

A common application for a structural angle is loading in the plane of the web with bending about the geometric axis perpendicular to the web. The more general form of the M_{cr} calculation given by Equation 40 is required, which incorporates the term $(I_x I_y - I_{xy}^2)/I_x$ in place of I_y.

Figure 10 shows a general angle section with dimensional parameters and formulas for the required properties, including a direct formula for the expression $(I_x I_y - I_{xy}^2)/I_x$. A simple formula is provided for $\beta_x/2$, which is negative when the flange is on the positive y-side of the x-axis. The shear center is at the intersection of the angle legs; therefore, C_w can be taken as 0 (again assuming mid-line dimensions and thin-walled assumptions, thus ignoring fillets and secondary warping that result in quite small, but non-zero C_w).

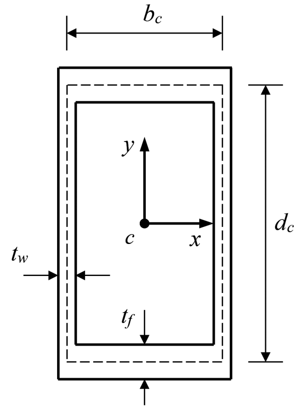

$$A = (b_c + t_w)(d_c + t_f) - (b_c - t_w)(d_c - t_f)$$

$$I_x = \frac{1}{12}(b_c + t_w)(d_c + t_f)^3 - \frac{1}{12}(b_c - t_w)(d_c - t_f)^3$$

$$I_y = \frac{1}{12}(d_c + t_f)(b_c + t_w)^3 - \frac{1}{12}(d_c - t_f)(b_c - t_w)^3$$

$$J = \frac{2b_c^2 d_c^2}{d_c/t_w + b_c/t_f}$$

$$\omega_{n,max} = \frac{b_c d_c (d_c/t_w - b_c/t_f)}{4(d_c/t_w + b_c/t_f)}$$

$$C_w = \frac{1}{3} A \omega_{n,max}^2$$

Fig. 6. Box section properties.

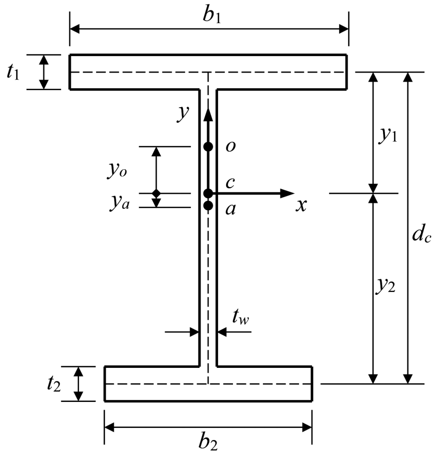

$$A = t_1 b_1 + t_2 b_2 + t_w d_c$$

$$y_1 = \left(t_2 b_2 d_c + \frac{1}{2} t_w d_c^2\right)/A \qquad y_2 = d_c - y_1$$

$$I_x = t_1 b_1 y_1^2 + t_2 b_2 y_2^2 + \frac{1}{3} t_w \left(y_1^3 + y_2^3\right)$$

$$I_y = \frac{1}{12} t_1 b_1^3 + \frac{1}{12} t_2 b_2^3 = I_{y1} + I_{y2}$$

$$J = \frac{1}{3}\left(b_1 t_1^3 + b_2 t_2^3 + d_c t_w^3\right)$$

$$y_o = \left(t_1 b_1^3 y_1 - t_2 b_2^3 y_2\right)/12 I_y$$

$$y_a = \begin{bmatrix} t_1 b_1 y_1 \left(b_1^2 + 12 y_1^2\right) - t_2 b_2 y_2 \left(b_2^2 + 12 y_2^2\right) \\ +3 t_w \left(y_1^4 - y_2^4\right) \end{bmatrix} \frac{1}{24 I_x}$$

$$\beta_x/2 = y_a - y_o$$

$$C_w = t_1 b_1^3 t_2 b_2^3 d_c^2 / 144 I_y = I_{y1} I_{y2} d_c^2 / I_y$$

Fig. 7. Mono-symmetric I-section properties.

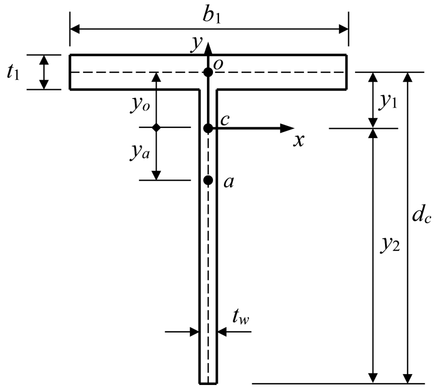

$$y_1 = \frac{t_w d_c^2}{2\left(t_1 b_1 + t_w d_c\right)} \qquad y_2 = d_c - y_1$$

$$I_x = t_1 b_1 y_1^2 + \tfrac{1}{3} t_w \left(y_1^3 + y_2^3\right)$$

$$I_y = \tfrac{1}{12} t_1 b_1^3$$

$$J = \tfrac{1}{3}\left(b_1 t_1^3 + d_c t_w^3\right) \qquad C_w \cong 0$$

$$y_o = y_1$$

$$y_a = \left[t_1 b_1 y_1 \left(b_1^2 + 12 y_1^2\right) + 3 t_w \left(y_1^4 - y_2^4\right)\right] / 24 I_x$$

$$\beta_x/2 = y_a - y_o$$

Fig. 8. Tee section properties.

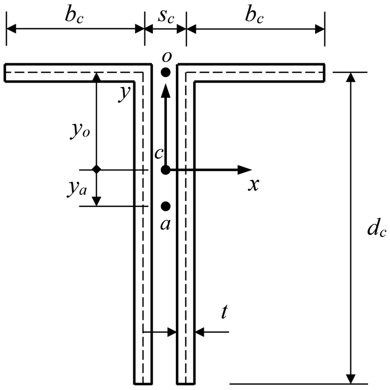

$$I_x = \frac{t d_c^3}{6}\left(\frac{4b_c + d_c}{b_c + d_c}\right) \qquad J = \tfrac{2}{3}(b_c + d_c)t^3$$

$$I_y = \frac{t}{6}\left[b_c^3 + 3b_c(s_c + b_c)^2 + 3d_c s_c^2\right]$$

$$y_o = \frac{d_c^2}{2(b_c + d_c)} \qquad C_w \cong 0$$

$$y_a = \frac{b_c^2(2b_c + 3s_c)(b_c + d_c) - 3b_c^2 d_c^2}{2d_c(b_c + d_c)(4b_c + d_c)}$$

$$\frac{\beta_x}{2} = y_a - y_o = \frac{(2b_c^2 - 2b_c d_c - d_c^2)(b_c + d_c) + 3b_c^2 s_c}{2d_c(4b_c + d_c)}$$

Fig. 9. Double-angle section properties.

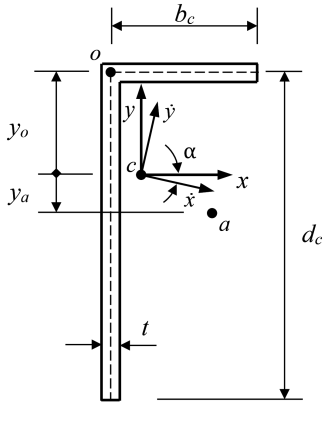

$$I_x = \frac{t d_c^3}{12}\left(\frac{4b_c + d_c}{b_c + d_c}\right) \qquad I_{xy} = \frac{t b_c^2 d_c^2}{4(b_c + d_c)}$$

$$I_y = \frac{t b_c^3}{12}\left(\frac{b_c + 4d_c}{b_c + d_c}\right) \qquad J = \tfrac{1}{3}(b_c + d_c)t^3$$

$$\frac{I_x I_y - I_{xy}^2}{I_x} = \frac{t b_c^3}{3}\left(\frac{b_c + d_c}{4b_c + d_c}\right) \qquad C_w \cong 0$$

$$y_o = \frac{d_c^2}{2(b_c + d_c)} \qquad y_a = -\frac{b_c(b_c^2 + 3d_c^2)}{8d_c(b_c + d_c)}$$

$$\frac{\beta_x}{2} = y_a - y_o = -\frac{4d_c^2 - b_c d_c + b_c^2}{8d_c}$$

Fig. 10. Single-angle section properties.

For bending about the principal $\dot{x}$-axis, the properties $I_{\dot{y}}$ and $\beta_{\dot{x}}/2$ are required, which are determined as follows:

$$I_{\dot{y}} = \frac{1}{2}(I_x + I_y) - \frac{1}{2}\sqrt{(I_x - I_y)^2 + 4I_{xy}^2} \tag{44}$$

$$\alpha = \frac{1}{2}\arctan\frac{-2I_{xy}}{I_x - I_y} \tag{45}$$

$$\frac{\beta_{\dot{x}}}{2} = \frac{\beta_x}{2}\cos\alpha - \frac{\beta_y}{2}\sin\alpha = \tag{46}$$

$$-\left(\frac{4d_c^2 - b_c d_c + b_c^2}{8d_c}\right)\cos\alpha - \left(\frac{4b_c^2 - b_c d_c + d_c^2}{8b_c}\right)\sin\alpha$$

For the special case of an equal leg angle, $I_{\dot{y}} = tb_c^3/12$, $\alpha = -\pi/4$, and $\beta_{\dot{x}}/2 = 0$. The major principal axis is an axis of symmetry and the simpler form of Equation 43 can be used.

General Built-Up Section

For any general section built up of other shapes, most section properties can be calculated from the properties of the individual shapes. Figure 11 shows an example built-up section and the method of calculating many of the properties.

Calculating the torsion constant J as the summation of the individual J values is conservative and often accurate enough, but built-up sections that form fully enclosed hollow regions will have much larger J values. This and other torsional properties (shear center and warping constant) are more difficult to calculate for a general section. Software tools that utilize numerical methods are recommended for determining these properties. As with the single angle section, bending about the non-principal x-axis would use Equation 40.

DISCUSSION OF AISC PROVISIONS

The elastic lateral-torsional buckling formulas in the AISC *Specification* (2022) are substantially based on Equation 39; however, many different formulas are given—uniquely customized and approximated for all the different types of standard sections. The accuracy of these elastic buckling formulas and approximations is examined in this section. Note, the objective of the AISC *Specification* is to provide a reliable nominal moment; however, here only the elastic lateral-torsional buckling portion of the calculation is assessed, and thus, the differences do not necessarily equate to meaningful strength reliability and only to accuracy of the elastic expressions.

Bending about Axis of Symmetry

AISC *Specification* Equation F2–4 is shown here as Equation 47 converted from stress to moment, applicable to doubly symmetric I-shapes and channels.

$$M_{cr} = \frac{C_b \pi^2 E S_x}{(L/r_{ts})^2}\sqrt{1 + 0.078\frac{Jc}{S_x h_o}\left(\frac{L}{r_{ts}}\right)^2} \tag{47}$$

$$r_{ts}^2 = \frac{\sqrt{I_y C_w}}{S_x} \tag{48}$$

$$c = 1 \text{ for I-shapes, } c = \frac{h_o}{2}\sqrt{\frac{I_y}{C_w}} \text{ for channels} \tag{49}$$

Equation 47 is identical to Equation 43 but restructured to use new variables r_{ts} and c, which are themselves defined as functions of I_y, C_w, S_x, and h_o. When the expressions for r_{ts} and c are substituted into this equation, the variables S_x

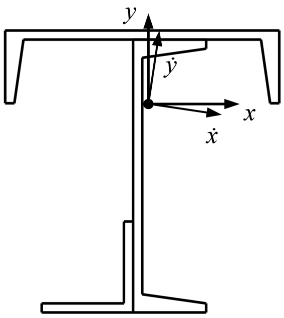

$$I_x = \int_A y^2\,dA = \sum I_{xi} + \sum A_i \bar{y}_i^2$$

$$I_y = \int_A x^2\,dA = \sum I_{yi} + \sum A_i \bar{x}_i^2$$

$$I_{xy} = \int_A xy\,dA = \sum I_{xyi} + \sum A_i \bar{x}_i \bar{y}_i$$

$$J = \sum J_i \quad \text{(conservative)}$$

$$y_a = \frac{U_x I_y - U_y I_{xy}}{2(I_x I_y - I_{xy}^2)}$$

$$U_x = \int_A y^3\,dA + \int_A x^2 y\,dA$$

$$U_y = \int_A x^3\,dA + \int_A y^2 x\,dA$$

Fig. 11. Built-up unsymmetrical section properties.

and h_o factor out entirely. These additional variables are unnecessary and even misleading in suggesting what properties control lateral-torsional buckling. It should also be noted that lateral-torsional buckling for other section types bending about an axis of symmetry as shown in Figure 5 are not addressed in Chapter F.

Mono-Symmetric I-Section

AISC *Specification* Equation F4-5 is shown here as Equation 50 converted from stress to moment, applicable to mono-symmetric I-shapes.

$$M_{cr} = \frac{C_b \pi^2 E S_x}{\left(L/r_t\right)^2}\sqrt{1+0.078\frac{J}{S_x h_o}\left(\frac{L}{r_t}\right)^2} \tag{50}$$

This is similar to Equation 47 but restructured to use the additional variable r_t, which is defined as a function of dimensional parameters of the section (i.e., the flange and a portion of the web). The square of r_t is intended to approximate $\sqrt{I_y C_w}/S_x$ combined with the influence of β_x. However, this approximation can lead to significant error compared to Equation 39 as illustrated in Figure 12. The use of r_t (and r_{ts} for doubly symmetric I-shapes) reverts to the pre-1986 concept of treating the compression flange as a column, which is no longer necessary given the availability of the relevant section properties or methods of calculating them. Further, the subtle difference between r_t and r_{ts} can lead to additional error/confusion.

The AISC *Specification* Commentary (2022) includes the theoretically based Equation C-F4-3 incorporating C_w and β_x and is equivalent to Equation 39. An accurate formula for C_w and an approximation for β_x are provided as functions of section depth and flange moments of inertia. Figure 12 shows this approach is more accurate than *Specification* Equation F4-5, although the β_x approximation increases the error for larger flanges.

AISC *Specification* Section F5 also applies to I-shapes but with slender webs. *Specification* Equation F5-4 is shown here as Equation 51, which is the same as Equation 50 with the exclusion of torsional constant J, and is therefore a more conservative approximation of M_{cr}.

$$M_{cr} = \frac{C_b \pi^2 E S_x}{\left(L/r_t\right)^2} \tag{51}$$

Square and Rectangular HSS and Box Sections

AISC *Specification* Equation F7-9 is shown here as Equation 52, applicable to closed doubly symmetric rectangular sections—that is, hollow structural sections (HSS) and box sections. This is equivalent to Equation 43 where substitutions have been made for $G = E/2.6$, $I_y = Ar_y^2$, $C_w = 0$, and $\pi/\sqrt{2.6}$ has been rounded up to 2. The assumption that $C_w = 0$ (i.e., negligible) is accurate for square HSS of uniform thickness, although C_w increases with aspect ratio for rectangular HSS. Torsional stiffness is dominated by pure torsion (GJ) for common HSS and box sections; hence, it is generally appropriate to ignore the negligible influence of C_w.

$$M_{cr} = 2EC_b\frac{\sqrt{JA}}{L/r_y} \tag{52}$$

Tees and Double Angles

AISC *Specification* Equation F9-10 is shown here as Equation 53, applicable to tees and double angles. Note that the bending coefficient C_b is not utilized in this equation as explained in the AISC *Specification* Commentary. For these sections, C_w is typically negligible and can be ignored. The new variable, B, in the AISC formula is a dimensionless value intended to represent $\left(\pi\beta_x/2L\right)\sqrt{EI_y/GJ}$ by (crudely)

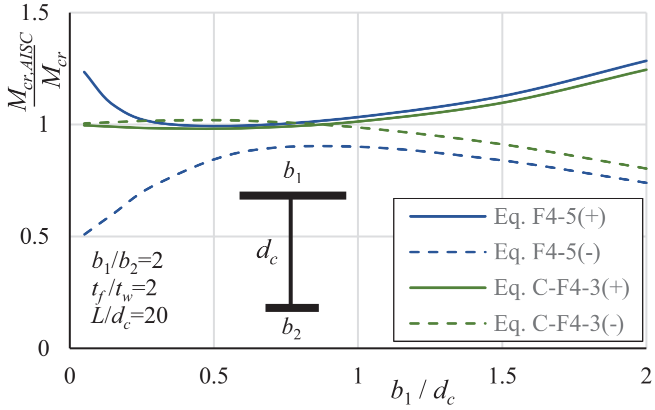

Fig. 12. AISC M_{cr} *equation accuracy for mono-symmetric I-sections.*

approximating β_x as $0.9y_2$. The error introduced by this approximation is shown in Figure 13 for tee sections and Figure 14 for double-angle sections, as compared to Equation 39. For tee sections with $b_1/d_c > 1.5$ and double angles with $b/d > 1$, the error is significant. The error for double angles increases as the spacing between them increases.

$$M_{cr} = \frac{1.95E}{L_b}\sqrt{I_y J}\left(B + \sqrt{1+B^2}\right) \tag{53}$$

$$B = \pm 2.3\frac{y_2}{L}\sqrt{\frac{I_y}{J}} \tag{54}$$

Single Angle

AISC *Specification* Equation F10-4 is shown here as Equation 55, applicable to single angles bending about their major principal axis. This is equivalent to Equation 39, where substitutions have been made for $G = E/2.6$, $I_{\dot{y}} = Ar_{\dot{y}}^2$, $J = At^2/3$, and $C_w = 0$. Values for $\beta_{\dot{x}}$ are provided in AISC *Specification* Commentary Table C-F10.1 as β_w for common angle sizes independent of thickness. These values are accurate for $b/t = 16$, where b is the longer leg. For b/t other than 16, some small error is introduced.

$$M_{cr} = 1.125\frac{C_b E A r_{\dot{y}} t}{L}\left[\pm 4.4\frac{\beta_{\dot{x}} r_{\dot{y}}}{Lt} + \sqrt{\left(4.4\frac{\beta_{\dot{x}} r_{\dot{y}}}{Lt}\right)^2 + 1}\right] \tag{55}$$

AISC *Specification* Equations F10-5a and 5b are shown here as Equation 56, applicable to equal leg angles bending about the geometric x-axis. This is equivalent to Equation 40, where substitutions have been made for $G = E/2.6$, $(I_x I_y - I_{xy}{}^2)/I_x = 2tb_c{}^3/15$, $J = 2b_c t^3/3$, $C_w = 0$, $\beta_x/2 = -b_c/2$, $b = b_c + t/2$, and $t = b/16$. For b/t other than 16, some small error is introduced. AISC *Specification* Section F10 has no provisions for an unequal leg angle bending about a geometric axis.

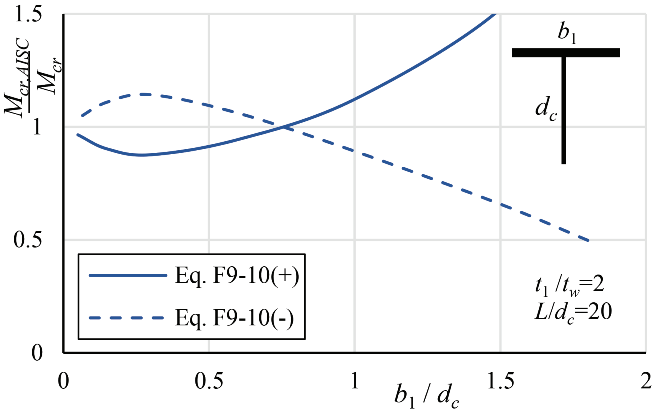

Fig. 13. AISC M_{cr} *equation accuracy for tee sections.*

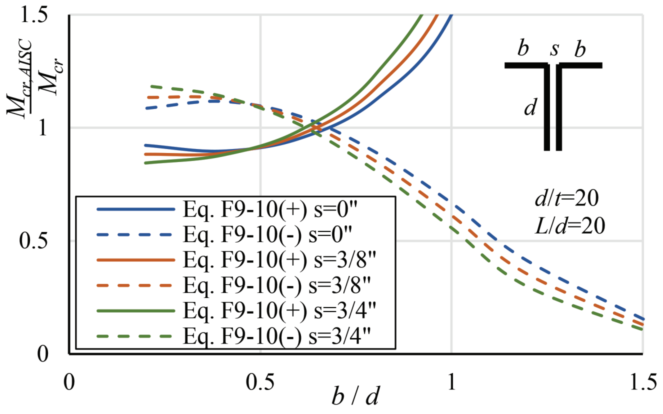

Fig. 14. AISC M_{cr} *equation accuracy for double-angle sections.*

$$M_{cr} = 0.58\frac{C_b E b^4 t}{L^2}\left[\pm 1 + \sqrt{0.88\left(\frac{Lt}{b^2}\right)^2 + 1}\right] \tag{56}$$

Unsymmetrical Sections

AISC *Specification* Section F12 offers no formula to determine M_{cr} for an unsymmetrical section and must therefore be determined by analysis. It is important to note that Equation 40 is valid for unsymmetrical sections, so the task is simply to determine the required properties of the cross section. Although this can be difficult for the torsional properties, section property software tools are available to assist if necessary. Then a more rigorous elastic beam analysis is not necessary.

Recommendations

The AISC *Specification* (2022) presents several different formulas for calculating M_{cr}, with the use of additional variables and approximations. The authors assert that it would be more useful and instructive to provide one general formula to the designer, applicable to any cross section, in the main body of the *Specification*—and provide design aids, or user notes where appropriate, for how the expression simplifies under certain assumptions (cross-section types). Specifically, we recommend that the *Specification* provide Equation 40 for the elastic lateral-torsional buckling moment bending about the geometric x-axis, repeated here for clarity:

$$M_{cr} = C_b \frac{\pi^2 E\left(I_x I_y - I_{xy}^2\right)}{L^2 I_x} \left[C_s \frac{\beta_x}{2} + \sqrt{\left(\frac{\beta_x}{2}\right)^2 + \frac{\left(GJL^2 + \pi^2 E C_w\right) I_x}{\pi^2 E\left(I_x I_y - I_{xy}^2\right)}}\right] \tag{57}$$

For sections where the geometric axes coincide with the principal axes, $I_{xy} = 0$ and the buckling formula can be expressed as:

$$M_{cr} = C_b \frac{\pi^2 E I_y}{L^2}\left[C_s \frac{\beta_x}{2} + \sqrt{\left(\frac{\beta_x}{2}\right)^2 + \frac{GJL^2}{\pi^2 E I_y} + \frac{C_w}{I_y}}\right] \tag{58}$$

If the x-axis is also an axis of symmetry, the shear center and asymmetry point lie on the x-axis ($y_o = y_a = 0$), thus $\beta_x/2 = 0$ and the buckling formula further simplifies to:

$$M_{cr} = C_b \frac{\pi}{L}\sqrt{E I_y\left(GJ + \frac{\pi^2}{L^2} E C_w\right)} \tag{59}$$

The recommendation is to provide Equation 57, along with the simplified formulas for the special cases associated with Equations 58 and 59. For all the common sections covered in AISC *Specification* (2022) Chapter F, closed-form equations have been provided herein for calculating all the necessary section properties (I_x, I_y, I_{xy}, J, C_w, y_o, y_a, $\beta_x/2$), and most of these properties are tabulated in the AISC *Manual* (2023). The addition of $\beta_x/2$ in the torsion property tables would fulfill the section properties requirements. For other sections, formulas can be derived, or software tools utilizing numerical methods may be used.

CONCLUSIONS

The elastic lateral-torsional buckling moment, M_{cr}, for a linear prismatic beam is a single formula applicable to any cross section. Properties of the cross section are required to calculate this buckling moment, including the St. Venant torsional constant, J, and warping constant, C_w. In addition, the less common asymmetry property β_x is required and involves some care in calculation. For sections symmetric about the axis of bending, β_x is zero, and the lateral-torsional buckling moment calculation is greatly simplified.

This article provides formulas for directly calculating β_x for many standard shapes using centerline dimensions and thin-wall assumptions. This includes mono-symmetric I-sections, tee sections, double-angle sections, and single-angle sections. For sections bending about a non-principal axis, such as single angles or unsymmetrical built-up sections, the buckling formula is essentially the same except that the minor axis moment of inertia must be generalized to incorporate the product of inertia.

The AISC *Specification* provisions for lateral-torsional buckling consist of different formulas for the various types of standard shapes, where additional variables and formulas are used to approximate β_x rather than calculating the actual values. These approximations introduce errors in the calculation of M_{cr} that can be unacceptably large. The removal of these approximations is recommended. The preferred alternative is to include the β_x property in all the torsional property tables in the next edition of the AISC *Manual*. Such tabulated values could be more accurately determined using direct integration of the cross-section properties to account for fillets and other features not incorporated in the typical mid-line, thin-walled properties. The section property formulas provided herein would also be helpful to include in a future edition of the AISC *Specification* Commentary or the AISC *Manual*.

For unsymmetrical or built-up sections, the calculation of torsional properties and β_x are more difficult. Software tools using numerical methods are available to calculate these properties. In addition, though not detailed herein, finite element software can be used to model and calculate M_{cr}, not only for unique cross sections, but also for other conditions that affect elastic stability, such as pre-buckling displacements, nonuniform moment, unusual boundary conditions, shear stresses, and load height.

REFERENCES

AISC (1923), *Standard Specification for Structural Steel Buildings*, American Institute of Steel Construction, New York, N.Y.

AISC (1936), *Specification for the Design, Fabrication and Erection of Structural Steel Buildings*, American Institute of Steel Construction, New York, N.Y.

AISC (1946), *Specification for the Design, Fabrication and Erection of Structural Steel Buildings*, American Institute of Steel Construction, New York, N.Y.

AISC (1961), *Specification for the Design, Fabrication and Erection of Structural Steel Buildings*, American Institute of Steel Construction, New York, N.Y.

AISC (1981), *Manual of Steel Construction*, 8th Ed., American Institute of Steel Construction, Chicago, Ill.

AISC (1986), *Specification for Structural Steel Buildings—Load and Resistance Factor Design*, American Institute of Steel Construction, Chicago, Ill.

AISC (2022), *Specification for Structural Steel Buildings*, ANSI/AISC 360–22, American Institute of Steel Construction, Chicago, Ill.

AISC (2023), *Steel Construction Manual*, 16th Ed., American Institute of Steel Construction, Chicago, Ill.

Bradford, M.A. (1992), “Lateral-Distortional Buckling of Steel I-Section Members,” *Journal of Constructional Steel Research*, Vol. 23.

CEN (2005), *Eurocode 3: Design of Steel Structures*, EN 1993, The European Committee for Standardization, Brussels, Belgium.

Commissioners of Railways (1848), *Report of the Commissioners of Railways*, London, England.

Euler, L. (1744), *Methodus Inveniendi Lineas Curvas*, Lausannæ & Genevæ, Apud Marcum-Michaelem Bousquet & Socios.

Glauz, R.S. (2017), “Elastic Lateral-Torsional Buckling of General Cold-Formed Steel Beams under Uniform Moment,” *Thin-Walled Structures*, Vol. 119.

Helwig, T.A., Frank, K.H., and Yura, J.A. (1997), “Lateral-Torsional Buckling of Singly-Symmetric I-Beams,” *Journal of Structural Engineering*, ASCE, Vol. 123.

Kirby, P.A. and Nethercot, D.A. (1979), *Design for Structural Stability*, John Wiley & Sons, Inc., New York, N.Y.

Liang, C., Reichenbach, M.C., Helwig, T.A., Engelhardt, M.D., and Yura, J.A. (2022), “Effects of Shear on the Elastic Lateral Torsional Buckling of Doubly Symmetric I-Beams,” *Journal of Structural Engineering*, Vol. 148.

Liu, S.W., Ziemian, R.D., Chen, L., and Chan, S.L. (2018), “Bifurcation and Large-Deflection Analyses of Thin-Walled Beam-Columns with Non-Symmetric Open-Sections,” *Thin-Walled Structures*, Vol. 132.

MSASect2 (2023), Matrix Structural Analysis for Arbitrary Cross-Sections, Version 1.0.6, Liu, S.W. and Ziemian, R.D. https://www.github.com/zsulsw/MSASect2.

Salmon, C.G. and Johnson, J.E. (1980), *Steel Structures: Design and Behavior*, 2nd Ed., Harper & Row, New York, N.Y.

ShapeBuilder (2023), Geometric and Structural Properties of Cross Sections, Version 14.0, IES, Inc. https://www.iesweb.com/sb.

Sectionproperties (2024), Open Source Python Package for the Analysis of Arbitrary Cross-Sections Using the Finite Element Method, Version 3.2.1, van Leeuwen, R. https://sectionproperties.readthedocs.io.

Timoshenko, S.P. (1936), *Theory of Elastic Stability*, 1st Ed., McGraw-Hill Book Co., New York, N.Y.

Timoshenko, S.P. and Gere, J.M. (1961), *Theory of Elastic Stability*, 2nd Ed., McGraw-Hill, New York, N.Y.

Wong, E. and Driver, R. (2010), “Critical Evaluation of Equivalent Moment Factor Procedures for Laterally Unsupported Beams,” *Engineering Journal*, AISC, Vol. 47, No. 1, pp.1–20.

Yu, W.W. (2000), *Cold-Formed Steel Design*, 3rd Ed., John Wiley & Sons, Inc., New York, N.Y.

Yura, J.A. (1995), “Bracing for Stability—State-of-the-Art,” *Proceedings of the ASCE Structures Congress XIII*, Boston, Mass., ASCE, New York, N.Y.

Strength Coefficients for Eccentrically Loaded Weld Groups

BO DOWSWELL

ABSTRACT

When AISC *Manual* Tables 8-4 through 8-11 are used to calculate the strength of eccentrically loaded weld groups with $F_{EXX} \neq 70$ ksi, the values are multiplied by an electrode strength coefficient, C_1. The C_1 values are dependent on the filler metal classification strength; however, they are not proportional to the filler metal classification strength ratio when $F_{EXX} \geq 80$ ksi. To consider the potential effect of reduced ductility, the C_1 values include reduction factors of 0.85 and 0.90 for higher-strength welds.

To investigate the accuracy of the electrode strength coefficients, the ductility of high-strength welds was evaluated using the data from 93 experimental tests from three existing research projects with $F_{EXX} > 70$ ksi. The data was used to plot the weld metal tensile strength versus the normalized rupture deformation of both longitudinal and transverse fillet welds. The analysis showed that, when $F_{EXX} \leq 120$ ksi, the C_1 values can be based solely on the filler metal classification strength ratio, $F_{EXX}/70$ ksi, without the reduction factors of 0.85 and 0.90 for higher-strength welds.

Keywords: eccentrically loaded weld groups, electrode strength coefficient, weld ductility.

INTRODUCTION

AISC *Steel Construction Manual* (2023) Tables 8-4 through 8-11 are used to calculate the strength of eccentrically loaded weld groups. The tables were developed using the instantaneous center of rotation (ICR) method with a filler metal classification strength, F_{EXX}, of 70 ksi. For other filler metal strengths, Table 8-3 provides electrode strength coefficients, C_1, that are used with Tables 8-4 through 8-11. The C_1 values are dependent on the filler metal classification strength; however, they are not proportional to the filler metal classification strength ratio when $F_{EXX} \geq 80$ ksi. This results in a significant strength reduction for higher-strength welds, which is not required in either the AISC *Specification* (2022) or AWS D1.1 (2020a). Based on experimental tests, the accuracy of the electrode strength coefficients will be determined and revised values will be proposed.

AISC *MANUAL*

Part 8 of the AISC *Manual* discusses three methods to analyze eccentrically loaded weld groups: The ICR method, the elastic method and the plastic method. Both the elastic and plastic methods were developed theoretically. The ICR method was developed using a semi-empirical approach, with an empirical load-deformation curve for short segments within the weld group.

Because the ICR method is iterative, considerable design effort is required to calculate the strength of a weld group using this method. AISC *Manual* Tables 8-4 through 8-11 provide a simpler, noniterative design method by listing the appropriate coefficients for several different weld group geometries. The tables were developed using the equations in AWS D1.1 Subclause 4.6.4.3. These equations are also shown on AISC *Manual* pages 8-13 and 8-14. AWS D1.1 is based solely on ASD. The AISC *Manual* provides the nominal strength equations, which can be used with ASD and LRFD. The weld group strength is the sum of the strengths of each element within the group. The nominal stress in Element *i* is calculated with AISC *Manual* Equation 8-3.

$$F_{nwi} = 0.60 F_{EXX} \left(1.0 + 0.50 \sin^{1.5} \theta_i\right) \left[p_i \left(1.9 - 0.9 p_i\right)\right]^{0.3} \qquad \text{(\textit{Manual} Eq. 8-3)}$$

where $0.60F_{EXX}$ is the nominal stress for concentrically loaded fillet welds from AISC *Specification* Table J2.5. The first term in parentheses is the directional strength increase factor, which is identical to AISC *Specification* Equation J2-5 if θ_i is replaced with θ. The second bracketed term is a strain compatibility factor, which is dependent on the deformation ratio, p_i. The ratio of Element *i* deformation to its deformation at maximum stress is

$$p_i = \frac{\Delta_i}{\Delta_{mi}} \qquad \text{(\textit{Manual} Eq. 8-4)}$$

Bo Dowswell, PE, PhD, Principal, ARC International, LLC, Birmingham, Ala. Email: bo@arcstructural.com

Paper No. 2024-11

The deformation of Element i at maximum stress is

$$\Delta_{mi} = 0.209w(\theta_i + 2)^{-0.32}$$

(*Manual* Eq. 8-6)

The deformation of Element i at an intermediate stress level is

$$\Delta_i = \Delta_{ucr}\frac{r_i}{r_{cr}} \qquad (\textit{Manual}\text{ Eq. 8-5})$$

where Δ_{ucr} is the deformation of the weld element with the minimum Δ_{ui}/r_i ratio at ultimate (rupture) stress. The deformation of Element i at ultimate (rupture) stress is

$$\Delta_{ui} = 1.087w(\theta_i + 6)^{-0.65} < 0.17w$$

(*Manual* Eq. 8-7)

where

F_{EXX} = filler metal classification strength, ksi

r_{cr} = distance from the instantaneous center of rotation to the element with the minimum Δ_{ui}/r_i ratio, in.

r_i = distance from the instantaneous center of rotation to Element i, in.

w = weld leg size, in.

θ_i = angle between the longitudinal axis of weld element i and the direction of the resultant force acting on the element, degrees

BACKGROUND

This section of the paper will document background information related to the electrode strength coefficients. The ICR method will be briefly reviewed, followed by the implementation history of the electrode strength coefficients in the AISC *Manual*.

Instantaneous Center of Rotation Method

Butler et al. (1972) developed the ICR method based on the empirical load-deformation curves from Butler and Kulak (1971), who tested concentrically loaded fillet welds at angles of 0°, 30°, 60°, and 90° from the loading direction. The tests by Butler and Kulak as well as the tests on eccentrically loaded weld groups by Butler et al. used 60 ksi electrodes and ¼ in. fillet welds.

The ICR equations in both AWS D1.1 Subclause 4.6.4.3 and the AISC *Manual* were primarily developed by Lesik and Kennedy (1990). Lesik and Kennedy used linear regression to formulate the load-deformation curves with the data from Miazga and Kennedy (1989), who tested concentrically loaded 70 ksi fillet welds with varying load angles, θ, from 0 to 90° in 15° increments. These equations were used to plot the strength ratio, $F_{nw}/(0.6F_{EXX})$, versus normalized deformation, Δ/w, curves for θ = 0°, 30°, 60°, and 90° in Figure 1. An increase in θ results in a nonlinear strength increase based on the directional strength increase factor and a decrease in ductility based on AISC *Manual* Equation 8-7.

Lesik and Kennedy (1990) originally developed the strain compatibility factor as a polynomial function; however, their equation was replaced by the simpler empirical approximation in AISC *Manual* Equation 8-3. Also, an upper limit of $0.17w$ was added to their original equation for Δ_{ut}, resulting in AISC *Manual* Equation 8-7.

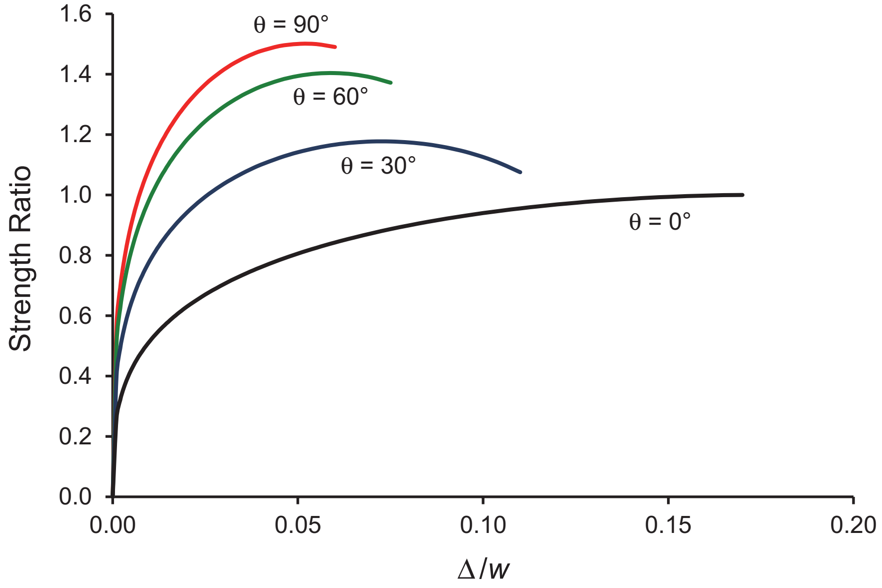

Fig. 1. Fillet weld strength ratio versus normalized deformation as a function of load angle, θ.

Table 1. Electrode Strength Coefficient, C_1

F_{EXX}	60	70	80	90	100	110
C_1	0.857	1.00	1.03	1.16	1.21	1.34
$\frac{F_{EXX}}{70\text{ ksi}}$	0.857	1.00	1.14	1.29	1.43	1.57
$\frac{C_1}{\left(\frac{F_{EXX}}{70\text{ ksi}}\right)}$	1.00	1.00	0.90	0.90	0.85	0.85

Electrode Strength Coefficient

The values in AISC *Manual* Tables 8-4 through 8-11 were calculated using $F_{EXX} = 70$ ksi. The strength of weld groups with other weld metal strengths can be calculated by adjusting the tabulated values by the electrode strength coefficient, C_1 in *Manual* Table 8-1.

The 6th Edition AISC *Manual* (1967) was the first to provide information on eccentrically loaded weld groups. The elastic method was used to develop design tables with $F_{EXX} = 60$ ksi. The weld group strengths for other filler metal classification strengths were calculated with the filler metal classification strength ratio, $F_{EXX}/60$ ksi. The 7th Edition *Manual* (AISC, 1973) used elastic design with $F_{EXX} = 70$ ksi; therefore, the weld group strength for other filler metal classification strengths was calculated with the filler metal classification strength ratio, $F_{EXX}/70$ ksi.

The 8th Edition *Manual* (AISC, 1980) was the first to publish design tables that were based on the ICR method. The development of these tables, which were also published in the 9th Edition *Manual* (AISC, 1989), was discussed by Tide (1980). The table coefficients were calculated with $F_{EXX} = 70$ ksi, and C_1 was used to calculate the weld group strength for other filler metal classification strengths, where $C_1 = F_{EXX}/70$ ksi.

For the 1st Edition LRFD *Manual* (AISC, 1986) and the 13th Edition combined ASD/LRFD *Manual* (AISC, 1992), as well as all later editions, the tables were based on the ICR method with $F_{EXX} = 70$ ksi. However, the value of C_1 included a reduction factor equal to either 0.90 (for 80 and 90 ksi welds) or 0.85 (for 100 and 110 ksi welds). These values are shown in Table 1.

The background of these reduction factors is ambiguous, and communication with members of past AISC *Manual* Committees (Thornton, 2020; Tide, 2020) revealed no further information. According to Butler et al. (1972), who originally developed the ICR method based on $F_{EXX} = 60$ ksi, "Because E60 and E70 electrodes have specified ultimate elongations nearly the same, it is felt that these results could be applied to connections made using E70 electrodes by proper consideration of the increase in electrode strength. The method could be used for fillet welds made from electrodes other than E60 and E70 by ascertaining the load-deformation response for these welds."

An accurate solution relies on sufficient ductility of the critical segment for load redistribution without rupture. The reduction factors were likely implemented in the AISC *Manual* because higher-strength welds are less ductile than E60 and E70 welds. However, in 1986 when these reduction factors were first published, experimental strength versus deformation data was unavailable for welds with F_{EXX} greater than 70 ksi.

DUCTILITY OF HIGH-STRENGTH WELDS

To investigate the accuracy of the electrode strength coefficients, the ductility of high-strength welds will be evaluated. After the modified coefficients were first published in 1986, a significant amount of experimental strength-versus-deformation data has become available for welds with F_{EXX} greater than 70 ksi.

Because transverse fillet welds have significantly less deformation capacity than longitudinal fillet welds, the ductility of transverse high-strength welds are the primary concern. In weld groups with both longitudinal and transverse welds, the longitudinal weld strength will be limited by the ductility of the transverse weld. According to the AWS D1.1 equation for rupture deformation (which is identical to AISC *Manual* Equation 8-7), the normalized rupture deformations for longitudinal and transverse welds are $\Delta_{ui}/w = 0.17$ and $\Delta_{ui}/w = 0.056$, respectively.

Figure 2 shows a plot of the weld metal tensile strength versus the normalized rupture deformation, Δ_u/w, of fillet welds. The data are from the 93 experimental tests on high-strength longitudinally and transversely loaded fillet welds by Collin and Johansson (2005), Bjork et al. (2012), and Sun et al. (2019). The red × data points represent transverse welds, and the blue hollow circles represent longitudinal welds. The red and blue vertical dashed lines represent the AWS normalized rupture deformations for longitudinal and transverse welds, respectively. It can be observed that, for tensile strengths less than 120 ksi, the AWS D1.1 equation for rupture deformation (which is identical to AISC

Manual Equation 8-7) generally provides conservative estimates of the normalized rupture deformation.

The average normalized deformations from this data are listed in Table 2. The data for 60 ksi welds from Butler and Kulak (1971) are also listed. A comparison of the rupture deformations shows that, for longitudinal welds, the rupture deformation of high-strength welds is 68% of that of 60 ksi welds; however, the rupture deformation of transverse welds is independent of strength. Because the shape of the load-deformation curves for high-strength welds is similar to that of 60 ksi welds, high-strength longitudinal welds in weld groups will reach a higher proportion of their rupture load compared to 60 ksi welds. The average transverse-to-longitudinal normalized deformation ratio for lap joints is $0.103/0.284 = 0.363$, which is similar to the value calculated with AISC *Manual* Equation 8-7: $0.056/0.17 = 0.33$.

Load-Deformation Curves

An evaluation of the load-deformation curves can provide further information on the behavior of high-strength fillet welds. The equations developed by Neis (1985) explicitly compensate for the effect of reduced weld metal ductility on the behavior. Neis used plasticity theory to derive the ultimate strength and maximum displacement of fillet welds. Although several simplifying assumptions were required, limited comparisons with experimental results showed "an acceptable fit." The ultimate (rupture) force and normalized deformation are calculated with Equations 1 and 2, respectively.

$$R_u = \sigma_{tu} w L \sqrt{\frac{1+15\sin^2\alpha_d}{6\left(1+7\sin^2\alpha_d\right)}} \tag{1}$$

$$\delta_u = \varepsilon_u \sqrt{\frac{3}{2\left(1+7\sin^2\alpha_d\right)}} \tag{2}$$

The load-deformation curve can be plotted with Equations 3 through 5.

$$R_i = R_u \frac{f_i}{f_u} \tag{3}$$

$$f_i = 1 - \frac{e^{-25\delta_i} + e^{-75\delta_i}}{2} \tag{4}$$

$$f_u = 1 - \frac{e^{-25\delta} + e^{-75\delta_u}}{2} \tag{5}$$

As a conservative estimate, the authors noted that the true tensile rupture stress can be calculated with Equation 6.

$$\sigma_{tu} = \sigma_u\left(1+0.75\varepsilon_u\right) \tag{6}$$

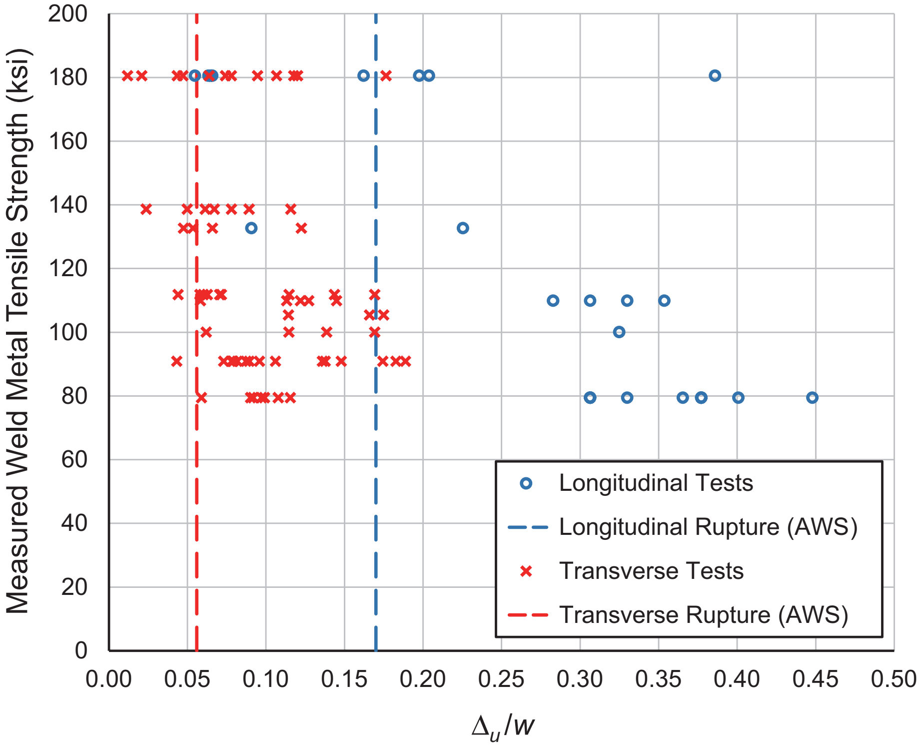

Fig. 2. Weld metal tensile strength versus normalized rupture deformation.

Table 2. Average Normalized Deformation

Joint Type	$F_{EXX} = 60$ ksi (Butler and Kulak, 1971)	High Strength ($F_{EXX} \approx 80$ to 180 ksi)	
	Average Δ_u/w	Number of Specimens	Average Δ_u/w
Longitudinal	0.420	26	0.284
Transverse (total)	—	67	0.0966
Transverse lap joints	0.104	36	0.103
Transverse T-joints	—	31	0.0889

Table 3. Minimum Elongation for All-Weld-Metal Tension Tests (%)

F_{EXX} ksi	Welding Process			
	SMAW	GMAW	FCAW	SAW
60	17 to 22	—	22	22
70	17 to 25	19 to 24	20 to 22	22
80	17 to 24	17 to 24	19	20
90	17 to 24	16 to 18	16 to 17	17
100	16 to 20	16	15 to 18	16
110	15 to 20	15	15	15
120	11 to 18	14 to 15	14	14

Equation 7 provides an approximate value of the angle between the weld longitudinal axis and the weld displacement direction.

$$\tan \alpha_d = \frac{\tan \theta}{4} \tag{7}$$

where

R_i = strength at deformation Δ_i, kips

L = weld length, in.

α_d = angle between the weld longitudinal axis and the weld displacement direction

Δ_i = deformation at an intermediate strength level, in.

Δ_u = ultimate (rupture) deformation, in.

δ_i = Δ_i/w

δ_u = Δ_u/w

ε_u = uniaxial engineering tensile rupture strain

σ_{tu} = true tensile rupture stress, ksi

σ_u = uniaxial engineering tensile rupture stress, ksi

The elongation requirements for carbon and low-alloy steels for shielded metal arc welding (SMAW), gas metal arc welding (GMAW), flux cored arc welding (FCAW) and submerged arc welding (SAW) welding processes from AWS A5.1 (2012), A5.5 (2014), A5.17 (2019), A5.18 (2017), A5.20 (2015), A5.23 (2011), A5.28 (2020b) and A5.29 (1998) are summarized in Table 3. Generally, weld metals exceed these requirements. For example, the average elongation measurements in Dowswell et al. (2021) Table 3.7 are 40 to 50% higher than the required minimum values in Table 3. These measurements are from all-weld-metal tensile tests with $F_{EXX} = 70$, 80 and 100 ksi.

The values in Table 4 are appropriate lower bounds for analyses with the Neis (1985) equations. The strength ratios, σ_{tu}/σ_u, in Table 4 are between 1.11 and 1.17. These values are similar to the constraint factor by Miazga and Kennedy (1989), which is 1.14 when $\theta = 90°$.

The Butler and Kulak (1971) curves were scaled up from 60 ksi to 70 ksi and plotted in Figures 3 and 4 for longitudinal and transverse welds, respectively. These normalized load versus normalized deformation curves are for 70 ksi electrodes. The figures also include the AWS D1.1 and Neis (1985) equations. The figures show that the Neis curves provide a close approximation of the shape of the empirical curves of Butler and Kulak, while also resulting in rupture loads that are similar to the AWS D1.1 equations. Also, the Neis equations explicitly compensate for the effect of reduced weld metal ductility on the behavior. Therefore, the Neis curves can be used as a baseline to project the behavior of higher-strength weld metals.

Table 4. Variables for Neis (1985) Equations

F_{EXX} ksi	ε_u	σ_{tu} ksi	σ_{tu}/σ_u
70	0.22	81.6	1.17
80	0.19	91.4	1.14
90	0.17	101	1.12
100	0.16	112	1.12
110	0.15	122	1.11
120	0.14	133	1.11

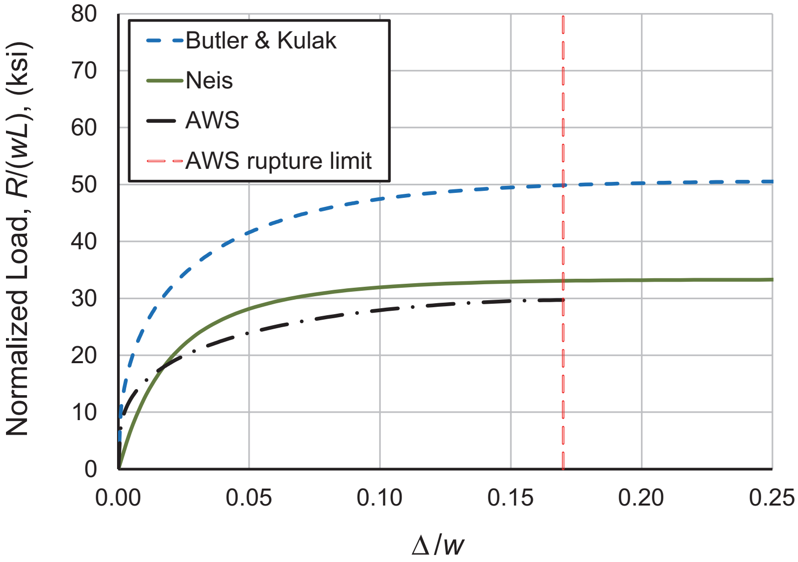

Fig. 3. Normalized load versus normalized deformation for 70 ksi longitudinal fillet welds.

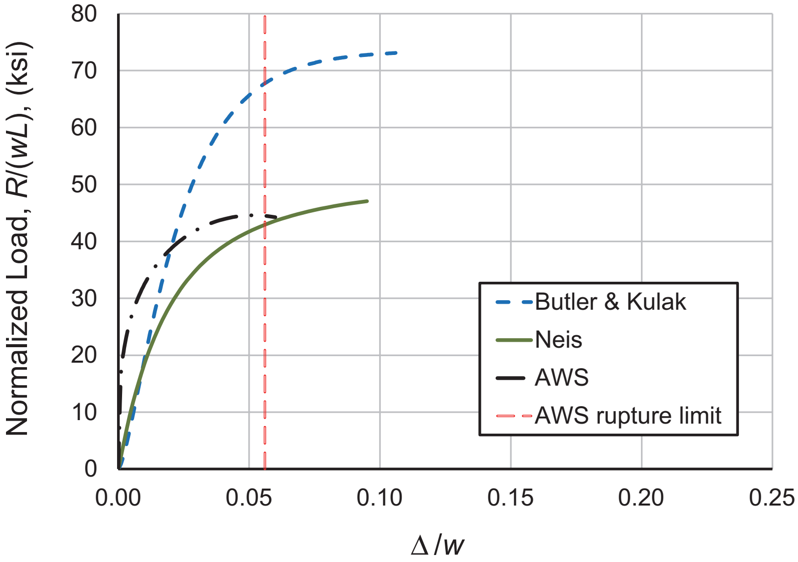

Fig. 4. Normalized load versus normalized deformation for 70 ksi transverse fillet welds.

For both the AWS D1.1 and Neis (1985) equations, the normalized load versus normalized deformation curves are plotted in Figures 5 and 6 for 70 ksi and 120 ksi electrodes, respectively. Generally, the AWS D1.1 curves are higher than the curves for transverse welds and lower than the Neis curves for longitudinal welds. Because the AWS D1.1 equations predict a similar, but more conservative, proportion of the longitudinal strength at the transverse rupture load, it can be concluded that the AWS D1.1 curves are conservative for both 70 ksi and 120 ksi electrodes.

SUMMARY AND CONCLUSIONS

When AISC *Manual* Tables 8-4 through 8-11 are used to calculate the strength of eccentrically loaded weld groups with $F_{EXX} \neq 70$ ksi, the values are multiplied by an electrode strength coefficient, C_1. The C_1 values are dependent on the filler metal classification strength; however, they are not proportional to the weld metal tensile strength ratio when $F_{EXX} \geq 80$ ksi.

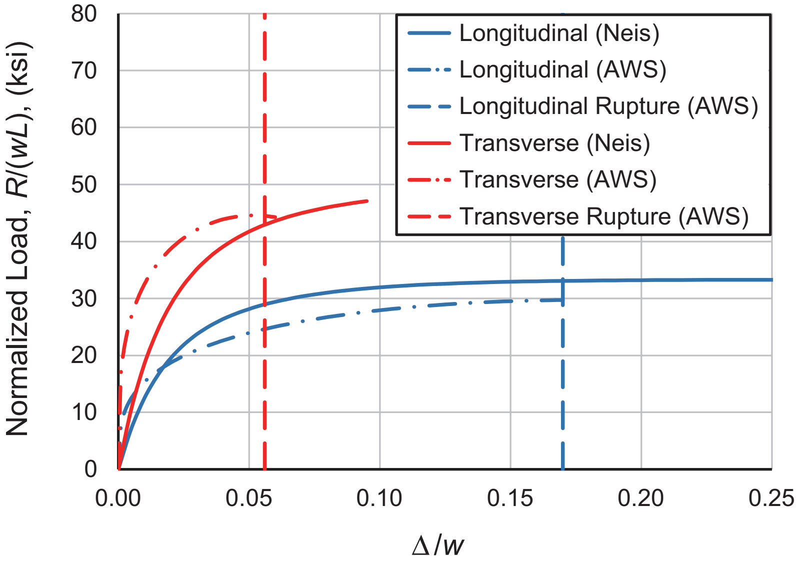

Fig. 5. Normalized load versus normalized deformation for 70 ksi fillet welds.

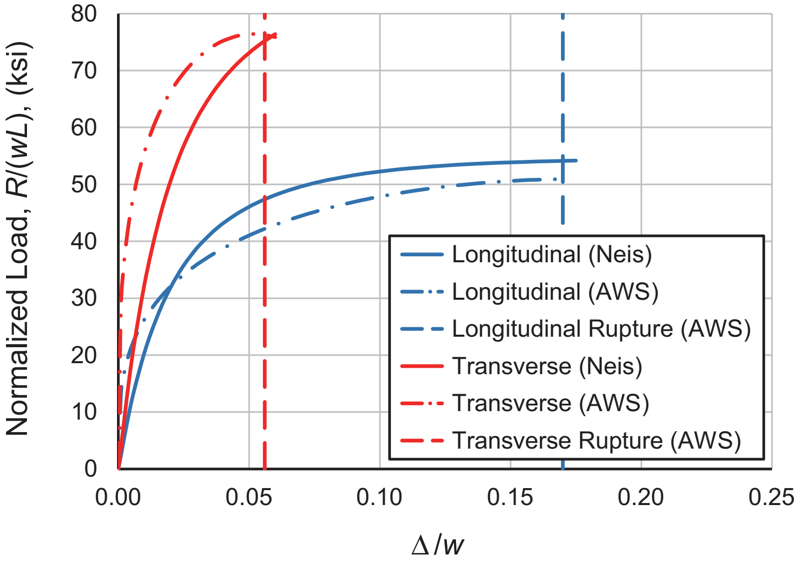

Fig. 6. Normalized load versus normalized deformation for 120 ksi fillet welds.

Table 5. Current and Proposed Values for the Electrode Strength Coefficient

F_{EXX}	60	70	80	90	100	110
Current	0.857	1.00	1.03	1.16	1.21	1.34
Proposed	0.857	1.00	1.14	1.29	1.43	1.57
$\frac{\text{Current}}{\text{Proposed}}$	1.00	1.00	0.90	0.90	0.85	0.85

An accurate solution relies on sufficient ductility of the critical segment for load redistribution without rupture. In 1986, when these modified electrode strength coefficients were first published, experimental strength-versus-deformation data were unavailable for welds with $F_{EXX} >$ 70 ksi. To consider the potential effect of reduced ductility, the C_1 values included reduction factors of 0.85 and 0.90 for higher-strength welds.

To investigate the accuracy of the electrode strength coefficients, the ductility of high-strength welds was evaluated. A significant amount of experimental strength-versus-deformation data is now available for welds with $F_{EXX} >$ 70 ksi. The data from the 93 experimental tests from three existing research projects were analyzed. The data were used to plot the weld metal tensile strength versus the normalized rupture deformation of both longitudinal and transverse fillet welds. The analysis showed that when $F_{EXX} \leq$ 120 ksi, the C_1 values can be based solely on the filler metal classification strength ratio, $F_{EXX}/70$ ksi, without the reduction factors of 0.85 and 0.90 for higher-strength welds. Both the current and proposed values for the electrode strength coefficient are listed in Table 5.

REFERENCES

AISC (1967), *Manual of Steel Construction*, 6th Ed., American Institute of Steel Construction, Chicago, Ill.

AISC (1973), *Manual of Steel Construction*, 7th Ed., American Institute of Steel Construction, Chicago, Ill.

AISC (1980), *Manual of Steel Construction*, 8th Ed., American Institute of Steel Construction, Chicago, Ill.

AISC (1986), *Manual of Steel Construction—Load and Resistance Factor Design*, 1st Ed., American Institute of Steel Construction, Chicago, Ill.

AISC (1989), *Manual of Steel Construction—Allowable Stress Design*, 9th Ed., American Institute of Steel Construction, Chicago, Ill.

AISC (1992), *Manual of Steel Construction—Volume II Connections*, ASD 9th Ed./LRFD 1st Ed., American Institute of Steel Construction, Chicago, Ill.

AISC (2022), *Specification for Structural Steel Buildings*, ANSI/AISC 360-22, American Institute of Steel Construction, Chicago, Ill.

AISC (2023), *Steel Construction Manual*, 16th Ed., American Institute of Steel Construction, Chicago, Ill.

AWS (1998), *Specification for Low-Alloy Steel Electrodes for Flux Cored Arc Welding*, AWS A5.29/A5.29M, American Welding Society, Miami, Fla.

AWS (2011), *Specification for Low-Alloy Steel Electrodes and Fluxes for Submerged Arc Welding*, AWS A5.23/A5.23M, American Welding Society, Miami, Fla.

AWS (2012), *Specification for Carbon Steel Electrodes for Shielded Metal Arc Welding*, AWS A5.1/A5.1M, American Welding Society, Miami, Fla.

AWS (2014), *Specification for Low-Alloy Steel Electrodes for Shielded Metal Arc Welding*, AWS A5.5/A5.5M, American Welding Society, Miami, Fla.

AWS (2015), *Specification for Carbon Steel Electrodes for Flux Cored Arc Welding*, AWS A5.20/A5.20M, American Welding Society, Miami, Fla.

AWS (2017), *Specification for Carbon Steel Electrodes and Rods for Gas Shielded Arc Welding*, AWS A5.18/A5.18M, American Welding Society, Miami, Fla.

AWS (2019), *Specification for Carbon Steel Electrodes and Fluxes for Submerged Arc Welding*, AWS A5.17/A5.17M, American Welding Society, Miami, Fla.

AWS (2020a), *Structural Welding Code—Steel*, AWS D1.1, American Welding Society, Miami, Fla.

AWS (2020b), *Specification for Low-Alloy Steel Electrodes and Rods for Gas Shielded Arc Welding*, AWS A5.28/A5.28M, American Welding Society, Miami, Fla.

Bjork, T., Toivonen, J., and Nykanen, T. (2012), "Capacity of Fillet Welded Joints Made of Ultra High-Strength Steel," *Welding in the World*, Vol. 56.

Butler, L.J. and Kulak, G.L. (1971), "Strength of Fillet Welds as a Function of Direction of Load," *Welding Research Supplement*, pp. 231–234.

Butler, L.J., Pal, S., and Kulak, G.L. (1972), "Eccentrically Loaded Welded Connections," *Journal of the Structural Division*, ASCE, Vol. 98, No. ST5.

Collin, P.P. and Johansson, P.B. (2005), "Design of Welds in High Strength Steel," *Proceedings of the Fourth European Conference on Steel and Composite Structures.*

Dowswell, B., Cox, C., Gallow, M.S., and Fouad, F.H. (2021), *Fillet and PJP Welds*, Final Report, American Institute of Steel Construction, Chicago, Ill.

Lesik D.F. and Kennedy, D.J.L. (1990), “Ultimate Strength of Fillet Welded Connections Loaded in Plane,” *Canadian Journal of Civil Engineering*, Vol. 17, No. 1, pp. 55–67.

Miazga, G.S. and Kennedy, D.J.L. (1989), “Behavior of Fillet Welds as a Function of the Angle of Loading,” *Canadian Journal of Civil Engineering*, Vol. 16, No. 4, pp. 583–599.

Neis, V.V. (1985), “New Constitutive Law for Equal Leg Fillet Welds,” *Journal of Structural Engineering*, Vol. 111, No. 8.

Sun, F.F., Ran, M.M., and Wang, Y.B. (2019), “Mechanical Behavior of Transverse Fillet Welded Joints of High Strength Steel Using Digital Image Correlation Techniques,” *Journal of Constructional Steel Research*, Vol. 162.

Thornton, W.A. (2020), Personal Communication.

Tide, R.H.R. (2020), Personal Communication.

Tide, R.H.R. (1980), “Eccentrically Loaded Weld Groups—AISC Design Tables,” *Engineering Journal*, AISC, Vol. 17, No. 4, pp. 90–95.

ERRATA

Torsion of Rectangular Connection Elements

BO DOWSWELL

Vol. 56, No. 2, 2019

In Example 1 on page 79, the nominal torsional strength is corrected to:

$$T_p = \frac{(0.6)(50\text{ ksi})(0.750\text{ in.})^2(15\text{ in.})}{2}\left[1+\frac{15\text{ in.}}{(2.4)(10\text{ in.})}\right]$$
$$= 206\text{ kip-in.}$$

And the available torsional strengths are updated to:

LRFD	ASD
$\phi T_p = (0.90)(206\text{ kip-in.})$ $= 185\text{ kip-in.}$	$T_p/\Omega = 206\text{ kip-in.}/1.67$ $= 123\text{ kips}$

On page 80, the interaction calculations are revised to:

For LRFD, interaction according to Equation 61 is:

$$\left(\frac{30\text{ kips}}{507\text{ kips}}\right)^2+\left(\frac{42.9\text{ kip-in.}}{185\text{ kip-in.}}\right)^2+\left(\frac{60.3\text{ kips}}{338\text{ kips}}\right)^4+\left[\left(\frac{600\text{ kip-in.}}{1{,}900\text{ kip-in.}}\right)^{1.7}+\left(\frac{60.0\text{ kip-in.}}{94.5\text{ kip-in.}}\right)^{1.7}\right]^{0.59} \tag{61}$$
$$= 0.800 < 1.0 \quad \textbf{o.k.}$$

For ASD, interaction according to Equation 61 is:

$$\left(\frac{20\text{ kips}}{337\text{ kips}}\right)^2+\left(\frac{28.6\text{ kip-in.}}{123\text{ kip-in.}}\right)^2+\left(\frac{40.2\text{ kips}}{225\text{ kips}}\right)^4+\left[\left(\frac{400\text{ kip-in.}}{1.260\text{ kip-in.}}\right)^{1.7}+\left(\frac{40.0\text{ kip-in.}}{62.9\text{ kip-in.}}\right)^{1.7}\right]^{0.59} \tag{61}$$
$$= 0.802 < 1.0 \quad \textbf{o.k.}$$

Guide for Authors

Scope *Engineering Journal* is dedicated to the improvement and advancement of steel construction. Its pages are open to all who wish to report on new developments or techniques in steel design, research, the design and/or construction of new projects, steel fabrication methods, or new products of significance to the uses of steel in construction. Only original papers should be submitted.

General Papers intended for publication should be submitted by email Margaret Matthew, editor, at **matthew@aisc.org**.

The articles published in the *Engineering Journal* undergo peer review before publication for (1) originality of contribution; (2) technical value to the steel construction community; (3) proper credit to others working in the same area; (4) prior publication of the material; and (5) justification of the conclusion based on the report.

All papers within the scope outlined above will be reviewed by engineers selected from among AISC, industry, design firms, and universities. The standard review process includes outside review by an average of three reviewers, who are experts in their respective technical area, and volunteers in the program. Papers not accepted will not be returned to the author. Published papers become the property of the American Institute of Steel Construction and are protected by appropriate copyrights. No proofs will be sent to authors.

Manuscripts Manuscripts must be provided in Microsoft Word format. Include a PDF with your submittal so we may verify fonts, equations and figures. View our complete author guidelines at **aisc.org/ej**.

Smarter. Stronger. Steel.

American Institute of Steel Construction
130 E Randolph St, Ste 2000, Chicago, IL 60601
312.670.2400 | aisc.org/ej